

AD_____

AWARD NUMBER: W81XWH-05-1-0396

TITLE: Angiogenic Signaling in Living Breast Tumor Models

PRINCIPAL INVESTIGATOR: Edward Brown

CONTRACTING ORGANIZATION: University of Rochester Medical Center
Rochester, NY 14642

REPORT DATE: June 2009

TYPE OF REPORT: Annual

PREPARED FOR: U.S. Army Medical Research and Materiel Command
Fort Detrick, Maryland 21702-5012

DISTRIBUTION STATEMENT: Approved for Public Release;
Distribution Unlimited

The views, opinions and/or findings contained in this report are those of the author(s) and should not be construed as an official Department of the Army position, policy or decision unless so designated by other documentation.

REPORT DOCUMENTATION PAGE				Form Approved OMB No. 0704-0188	
Public reporting burden for this collection of information is estimated to average 1 hour per response, including the time for reviewing instructions, searching existing data sources, gathering and maintaining the data needed, and completing and reviewing this collection of information. Send comments regarding this burden estimate or any other aspect of this collection of information, including suggestions for reducing this burden to Department of Defense, Washington Headquarters Services, Directorate for Information Operations and Reports (0704-0188), 1215 Jefferson Davis Highway, Suite 1204, Arlington, VA 22202-4302. Respondents should be aware that notwithstanding any other provision of law, no person shall be subject to any penalty for failing to comply with a collection of information if it does not display a currently valid OMB control number. PLEASE DO NOT RETURN YOUR FORM TO THE ABOVE ADDRESS.					
1. REPORT DATE 1 June 2009		2. REPORT TYPE Annual		3. DATES COVERED 1 Jun 2008 – 31 May 2009	
4. TITLE AND SUBTITLE Angiogenic Signaling in Living Breast Tumor Models				5a. CONTRACT NUMBER	
				5b. GRANT NUMBER W81XWH-05-1-0396	
				5c. PROGRAM ELEMENT NUMBER	
6. AUTHOR(S) . Edward Brown E-Mail: edward_brown@urmc.rochester.edu				5d. PROJECT NUMBER	
				5e. TASK NUMBER	
				5f. WORK UNIT NUMBER	
7. PERFORMING ORGANIZATION NAME(S) AND ADDRESS(ES) University of Rochester Rochester, NY 14642				8. PERFORMING ORGANIZATION REPORT NUMBER	
9. SPONSORING / MONITORING AGENCY NAME(S) AND ADDRESS(ES) U.S. Army Medical Research and Materiel Command Fort Detrick, Maryland 21702-5012				10. SPONSOR/MONITOR'S ACRONYM(S)	
				11. SPONSOR/MONITOR'S REPORT NUMBER(S)	
12. DISTRIBUTION / AVAILABILITY STATEMENT Approved for Public Release; Distribution Unlimited					
13. SUPPLEMENTARY NOTES					
14. ABSTRACT In this grant we propose to elucidate the signaling pathway that translates VEGFR activation into elevated vessel permeability, in endothelial cells within living breast tumor models. The working hypothesis is that the signaling pathway involved is a constitutively active form of the pathway shown for healthy mesenteric microvessels. Progress to date includes the training of personnel in the laboratory, the completion of instrumentation development for a novel method for the measurement of convective flow in tumors in vivo and extensive analysis of its capabilities, extensive investigation of breast tumor extracellular matrix using second harmonic generation, extensive analysis of the abilities of a novel permeability measurement technique and numerous preliminary experiments to establish methodology for tasks to commence in upcoming years.					
15. SUBJECT TERMS Angiogenesis, microscopy, signaling, VEGF, permeability					
16. SECURITY CLASSIFICATION OF:			17. LIMITATION OF ABSTRACT UU	18. NUMBER OF PAGES 68	19a. NAME OF RESPONSIBLE PERSON USAMRMC
a. REPORT U	b. ABSTRACT U	c. THIS PAGE U			19b. TELEPHONE NUMBER (include area code)

Table of Contents

Introduction.....	4
Body.....	4
Key Research Accomplishments.....	12
Reportable Outcomes.....	12
Conclusions.....	13
References.....	14
Appendices.....	15

Introduction

The goals of this grant are twofold: to explore signaling pathways that induce angiogenic phenotypes in endothelial cells within living breast tumor models, and to develop a series of optical techniques that contribute to this work, including second harmonic generation imaging of breast tumor collagen, and multiphoton fluorescence recovery after photobleaching (MP-FRAP) in the presence of convective flow. This is the conclusion of the fourth year of this grant and also the fourth year of my biomedical optics laboratory here at the University of Rochester Medical Center, a laboratory which consists of myself, Dr. Kelley Madden a Research Assistant Professor, Khawarl Liverpool a Technician, graduate students Ryan Burke, Javier Lapeira, Kelley Sullivan, and several students not funded by this award. Thanks to the Era of Hope Scholar Award we have made significant progress in our exploration of breast cancer and our development of optical techniques to advance its study. What follows is a discussion of our progress separated into three main themes

Body

Multiphoton Fluorescence Recovery After Photobleaching (MP-FRAP) with convective flow.

Task 7 of the statement of work focuses on the study of convection and diffusion in the transport of macromolecules away from a breast tumor vessel. This necessitated the development of a new experimental capability: the ability to measure macromolecular diffusion with three-dimensional resolution in deep tissue, in the presence of convective flow. Fortunately, MP-FRAP allows for the measurement of macromolecular diffusion with 3D resolution in deep tissue, and was in fact part of my Ph.D. thesis, so we were ideally suited to extend the capabilities of this technique to allow its application in the presence of convective flow. Over the past few years we have developed the theory for MP-FRAP with flow, evaluated its accuracy *in vitro* in artificial flow chambers, and *in vivo* in the angiogenic vasculature of breast tumors (vessels provide a “gold standard” for the flow velocity in the form of RBCs, so we can compare our measurements of plasma velocity to RBC velocity to evaluate accuracy). This has culminated in this month’s publication of **Sullivan K, Sipprell W, Brown E, Brown E. (2009) Improved model for multi-photon fluorescence recovery after photobleaching (MP-FRAP) expands the application of MP-FRAP within the in vivo environment. Biophysical Journal 96:5082-5094** which is reproduced at the end of this report. This past year in particular we performed extensive calculations on the ability of our new methodology to distinguish anomalous sub-diffusion from flow, determining that for any physiologically reasonable values of anomalous sub-diffusion parameters the effects are readily separable. Additionally, we repeated the experimental evaluation of the new MP-FRAP model’s accuracy, but with flow direction other than perpendicular to the optical axis, to verify its general utility.

This project has led to an interesting collaboration with Dr. Mitch Anthamatten from the University of Rochester Department of Chemical Engineering. He is a polymer scientist who is interested in developing shape memory polymers, materials who substantially change their physical properties in response to changes in temperature and force. While Dr. Anthamatten is interested in these materials for their own sake, I feel that these polymers have great promise as drug delivery vehicles: they could be implanted in the location of a primary tumor resection to slowly release therapeutic agents locally, or

implanted subcutaneously (as in Norplant) to slowly release anticancer or antimetastatic reagents systemically. The memory properties would then be particularly useful because reagent diffusion (and shape) properties could be greatly altered between the loading (*ex vivo*) and release (*in vivo*) steps. MP-FRAP is uniquely suitable to measure diffusion within these polymers because it can quantify diffusion with 3D resolution deep within the bulk gel, avoiding edge effects. This collaboration has culminated in the recent submission of **Li J, Sullivan K, Brown E, Anthamatten M. (2009) Thermally activated diffusion in reversibly associating polymers** and the submitted manuscript is reproduced at the end of this report.

Second Harmonic Generation in the breast tumor extracellular matrix

Task 9c of the statement of work focuses on the evaluation of the structural properties of the breast tumor extracellular matrix using second harmonic generation (SHG). SHG is the nonabsorptive combination of two excitation photons into one emission photon, “catalyzed” by a non-centrosymmetric medium such as a crystal surface, asymmetrically labeled membrane, or properly ordered fibers 1 (Fig. 1). Due to its coherent nature, SHG is intrinsically sensitive to molecular order.

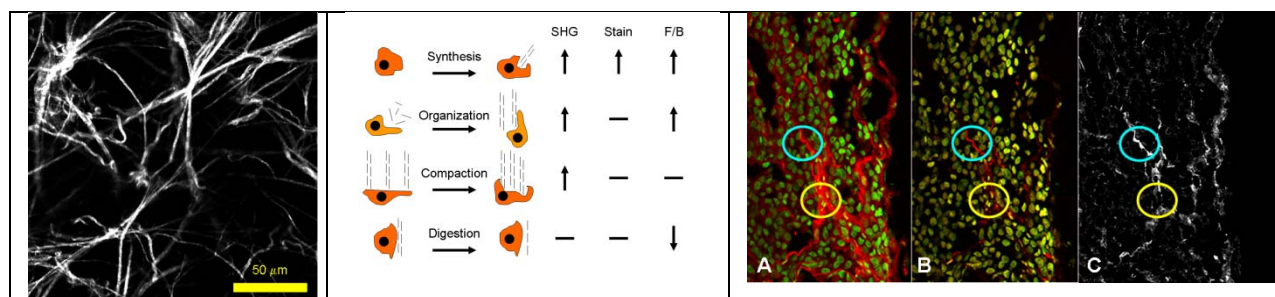


Figure 1. Left: SHG image of ordered collagen in an E0771 mammary tumor *ex vivo*.

Middle: Cartoon of ordering processes that can affect SHG. The most significant effects are shown.

Right: a: Tumor collagen immunofluorescence in red, **b:** SHG in red. **c:** SHG/IFC ratio. Green is a nuclear counterstain. Circled regions reveal differences in relative collagen organization.

Hence a canonical collagen fiber, containing triple helices tightly packed end-to-end in multiple parallel rows forming a cylindrical fibril, aligned with other fibrils in a bundle forming a fiber, is expected to produce significant SHG 2. Conversely, a region containing randomly oriented collagen triple helices which are not polymerized into a fibril is expected to produce little SHG. There are several mechanisms which can affect the SHG efficiency, all of which provide insight into the ordering of collagen in a region such as the $\sim 0.5 \mu\text{m}$ focal volume of a multiphoton laser-scanning microscope (MPLSM) (Fig. 1). SHG is only generated by highly ordered arrays of scatterers, so conversion of disordered collagen triple helices into ordered fibrils, or *de novo* synthesis of ordered fibrils can increase the SHG conversion efficiency within the focal volume. SHG efficiency scales with the square of the number of scatterers in the focal volume 1, therefore compaction of fibrils can increase the SHG efficiency. Lastly, the diameter of ordered fibrils dictates the ratio of forward-scattered to backward scattered SHG (F/B), as we demonstrated last year in breast tumor models in **Han et al Optics Express (2008)**.

In our work with SHG in breast tumor models over the past year as part of this award, we discovered some intriguing connections in the literature: the extent and nature of the ordering of

collagen fibers within a tumor has significant influence on the process of breast tumor metastasis. In murine breast tumor models, tumor cells move towards blood vessels along fibers that are visible via second harmonic generation 3, and SHG is exquisitely sensitive to molecular ordering (see above). Breast tumor cells that are moving along SHG-producing (i.e. ordered) collagen fibers move significantly faster than those cells that are moving independently of SHG-producing fibers 4, and the extent of SHG-associated tumor cell motility is correlated with metastatic ability of the breast tumor model 5. Furthermore, the tumor-host interface of murine breast tumor models is characterized by radially oriented SHG-producing fibers associated with tumor cells invading the surrounding tissue 6. Lastly, I have shown in earlier work that treatment of tumors with the hormone relaxin, known to alter metastatic ability, alters the collagen ordering as detectable by SHG 2.

To probe these intriguing connections between SHG and metastatic ability in breast tumors, we evaluated the tumor-averaged forward/backward SHG ratio of MDA-MB-231 and MDA-MB-361 tumors grown in Nude mice. These two tumors have markedly different metastatic phenotypes. As shown in Figure 2, the average SHG F/B ratio is also statistically significantly different, reinforcing the possibility that highly ordered (i.e. SHG-producing and high SHG F/B ratio) collagen fibers may encourage tumor metastasis.

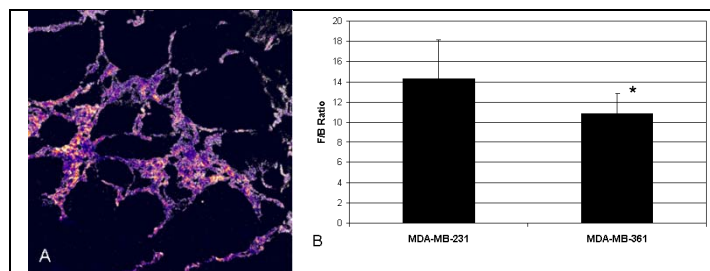


Figure 2 A: F/B ratio image of MDA-MB-231 grown in the mouse mammary fat pad. This image is a quantitative map of the length scale of ordering (corresponding to fibril diameter).

B: F/B ratio of highly metastatic MDA-MB-231 and less metastatic MDA-MB-361 tumors (mean ± S.D.). The differing F/B ratio ($P < 0.05$, $n = 9$ and 11) between metastatic phenotypes suggests that the F/B ratio will be useful as a method to quantify metastatic ability.

If the presence of ordered (SHG-producing) fibers encourages metastasis, it is desirable to dissect the cells and signals which encourage this ordering, so that they can be targeted and metastatic ability inhibited. To do this, we must first determine the responsible cells and signals by identifying promising candidates and then experimentally evaluating their impact on the ordering process. Analysis of our 2003 relaxin study 2, the only study in which collagen ordering in tumors has been directly biochemically altered, allows us to identify several such candidate cells and signals: since relaxin treatment altered

collagen ordering, the cells/pathways known to be activated by relaxin are candidates for cells/pathways involved in regulation of collagen ordering.

Relaxin binds macrophage glucocorticoid receptors, altering cytokine secretion 7. It inhibits TGF β 1-induced collagen gel contraction by fibroblasts 8, inhibits their differentiation into profibrotic myofibroblasts by inhibition of α SMA expression 9, and acts synergistically with EGF signaling 10, which inhibits gel contraction 11. Therefore our relaxin data suggests a macrophage/TGF β 1/EGF/fibroblast pathway as a key candidate pathway for control of collagen ordering as visualized by SHG. This is strongly supported by recent *in vivo* data in the developing mammary gland, where macrophages induce

assembly of collagen into ordered fibers, specifically inducing an increase in SHG signal around developing mammary buds with no alteration in collagen immunostaining 12.

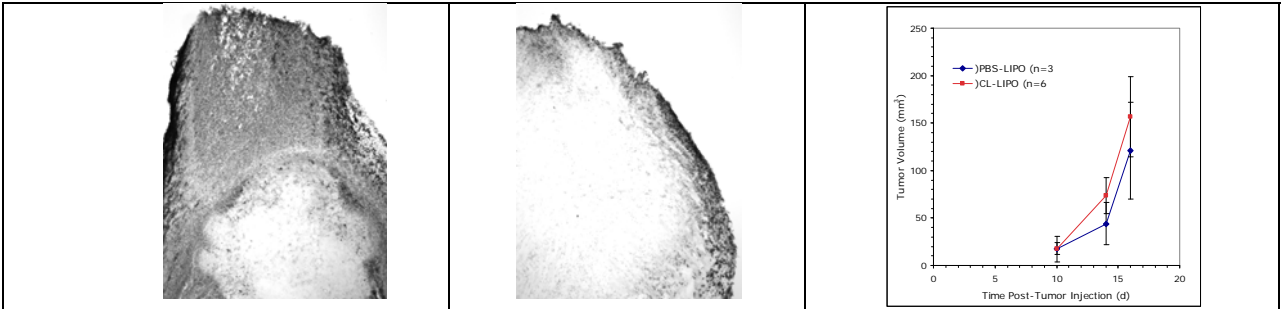


Figure 3. A: F4/80-stained E0771 tumor section from the MFP of a C57BL/6 mouse, 48 hours after the last treatment with PBS-loaded liposomes. Note the dark staining indicating presence of F4/80-expressing macrophages.

B: F4/80 stained E0771 from C57BL/6 MFP 48 hours after the last treatment with clodronate-loaded liposomes. Note reduction in the F4/80+ macrophage population as evidenced by the loss of staining. Images are 1 cm across.

C: Treatment has no affect on tumor growth. Animals were injected intraocularly with liposome solution every three to four days starting at the time of tumor cell injection

We therefore pursued macrophages as a possible source of “pro-ordering” signals that enhance tumor SHG. We grew E0771 murine mammary adenocarcinoma in the mammary fat pad of C57-BL6 mice and treated the animals for two weeks with either clodronate-liposomes or saline-liposomes as control. Liposomes are selectively taken up by macrophages and clodronate kills the macrophage. After two weeks of growth and treatment tumors were excised, fixed, sectioned and stained with anti-collagen antibodies. As SHG is sensitive to molecular ordering, while antibody staining is sensitive to number of epitopes, an SHG/staining ratio is an index of the local extent of molecular ordering. Some sections were stained for F4/80 to verify macrophage depletion. Lungs were excised, fixed, sectioned, and H+E stained to quantify metastasis. We found that clodronate treatment was effective at attenuating macrophages and did not affect primary tumor growth (Fig. 3). We also found that clodronate treatment causes a statistically significant change in average SHG ($p<0.05$), but no statistical

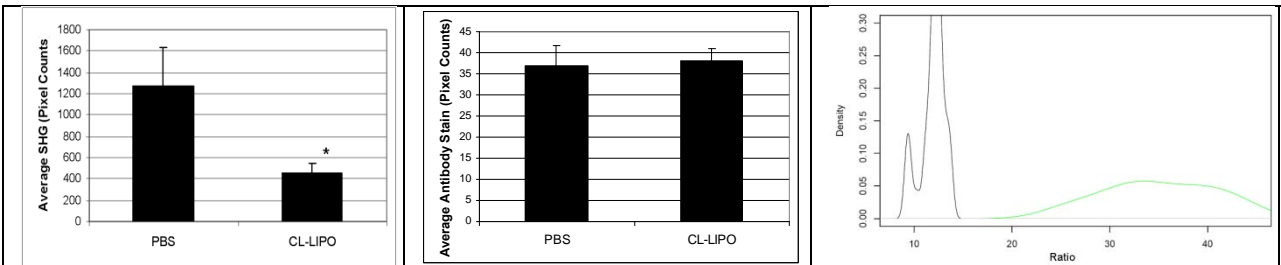
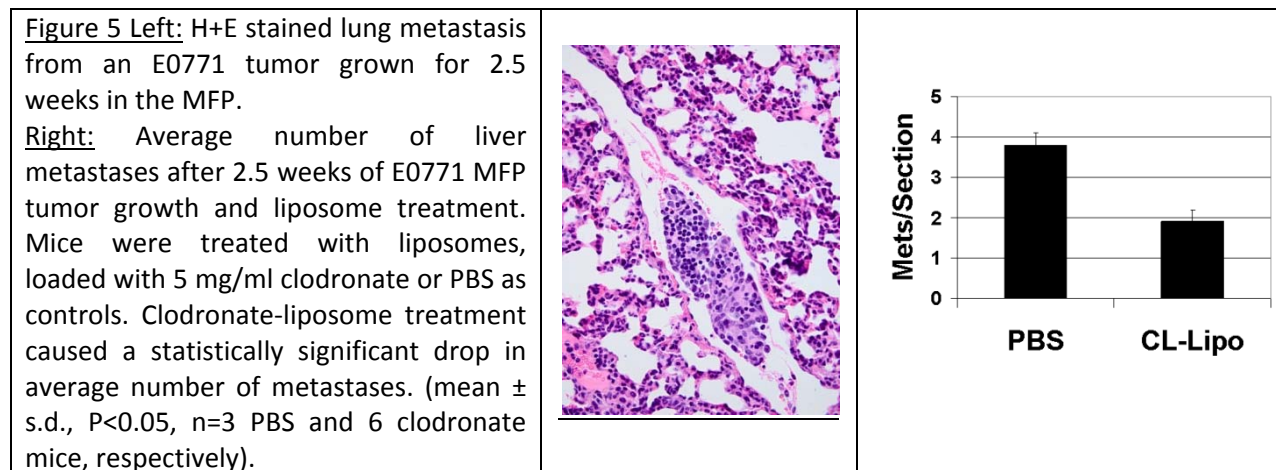


Figure 4 Left: Effect of macrophage depletion on average SHG in E0771 MFP tumors.

Center: Effect of macrophage depletion on average anti-collagen antibody staining in E0771 MFP tumors. (Mean± S.E.M.)

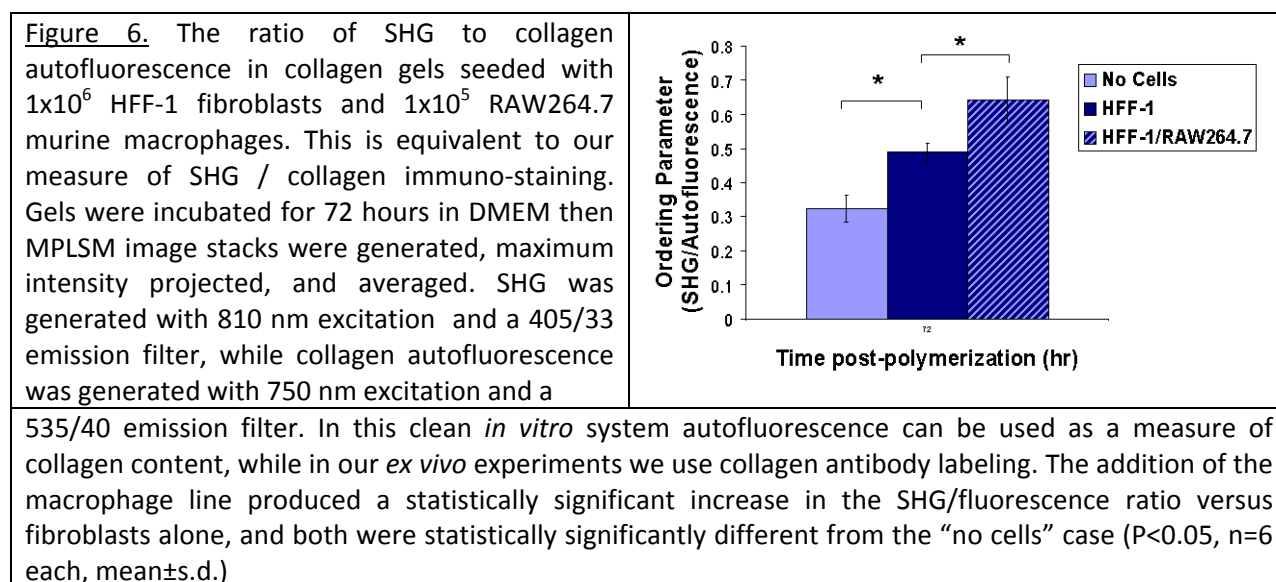
Right: Distribution of SHG/staining ratios in E0771 MFP tumors with and without macrophage ablation. Determined via Jackknife analysis, the distribution of the SHG/staining ratio for clodronate-treated E0771 MFP tumors (Black) does not overlap the distribution for PBS treated tumors (Green). This suggests that clodronate liposome treatment causes a decrease in SHG/staining ratio 13.

change in average staining ($p > 0.05$) using a standard t-test comparison (Fig. 4). The distribution of ratios of these two parameters as determined by Jackknife subsampling clearly does not overlap, suggesting that macrophage ablation causes a decrease in the SHG/staining ratio 13. Lastly, we found that clodronate treatment statistically significantly decreased the number of lung metastases (Fig. 5).



These experiments suggest that macrophages may influence collagen ordering in breast tumor models and hence influence metastatic ability. To probe the possible downstream mechanism we seeded collagen gels with either fibroblasts alone (the HFF-1 fibroblast line) or fibroblasts plus macrophages (the RAW264.7 line) and quantified the SHG/autofluorescence ratio as an index of relative collagen ordering (Fig. 6). While the fibroblasts alone statistically significantly enhanced the ordering index ($p < 0.05$), fibroblasts plus macrophages statistically significantly enhanced the ordering index more than fibroblasts alone ($p < 0.05$) suggesting that macrophages may influence collagen ordering through signaling with fibroblasts.

This exciting beginning is now being “spun off” as an independent ongoing project due to a successful application for an Era of Hope Scholar Research Award, commencing in September.



The influence of β -adrenergic signaling on breast tumor growth and angiogenesis

Tasks 1-6 of the statement of work focus on the dissection of signaling steps leading to VEGF-induced angiogenic phenotypes in endothelial cells in tumors. As part of this work we have recently been exploring the factors upstream of VEGF, leading to its enhanced expression in the tumor microenvironment. In clinical and animal studies, exposure to emotional stressors can increase solid tumor growth, including breast cancer 14. The catecholamines norepinephrine (NE) and epinephrine (EPI) are important stress neurotransmitters that communicate with target cells via α - and β -adrenergic receptors (AR). NE and EPI have recently been implicated as tumor growth promoters by stimulating angiogenesis, the growth of new blood vessels into a tumor 15,16. Angiogenesis is induced by vascular endothelial growth factor (VEGF) and other proangiogenic mediators, and VEGF mRNA is upregulated in some breast tumors by β -AR stimulation 15. We (and others) feel that this is an exciting and underappreciated avenue to affect breast tumor growth and angiogenesis: via the influence of emotional stress on adrenergic signaling and subsequent VEGF expression. This leads to a series of questions: does β -adrenergic signaling occur in breast tumor? If so, how heterogeneous is it? What are the downstream effector molecules? And lastly, is this pathway activated by emotional stress?

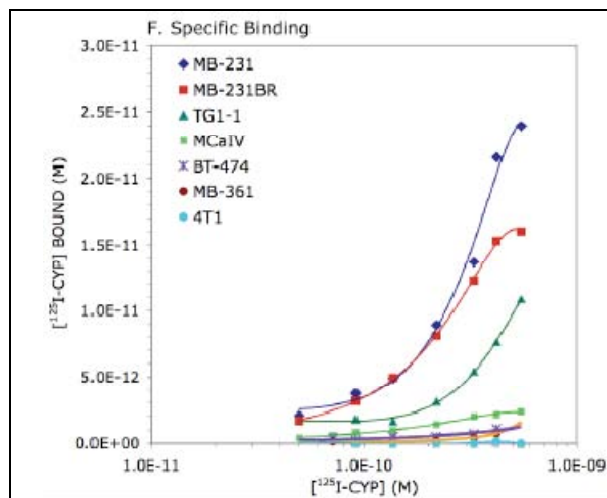


Figure 7. Heterogeneity of β -AR expression in breast cancer cell lines. Binding of the radiolabeled β -AR antagonist $[^{125}\text{I}]\text{-CYP}$ was measured in 4T1, MB-231, MB-231BR, MCalV, and MB-361. Specific binding at each ligand concentration was calculated by subtracting radioligand binding in the presence of unlabeled antagonist CGP-12177 from total ICYP binding. All binding curves were fit to a 3rd order polynomial equation. Results are representative of 2-3 experimental repetitions.

To explore the contribution of this pathway in angiogenic signaling in breast tumors we first quantified the number of β -adrenergic receptors in a panel of breast tumor cell lines (Fig. 7). The cell lines revealed significant heterogeneity in β -AR expression. We next quantified the efficiency of coupling of β -AR to its intracellular signaling pathway by quantifying cAMP expression after stimulation of the β -AR agonist Isoproterenol (ISO) (Fig. 8). In 5 out of 7 cell lines, cAMP production correlated with β -AR expression, but in two of the cell lines that express β -AR, β -AR stimulation did not elicit increased intracellular cAMP. Differences in β -AR signaling capacity were not due to differences in adenylate cyclase activity, as direct activation of adenylate cyclase with forskolin did not elicit similar differences in cAMP production (Fig. 8). To explore possible mechanisms underlying differences in total cAMP

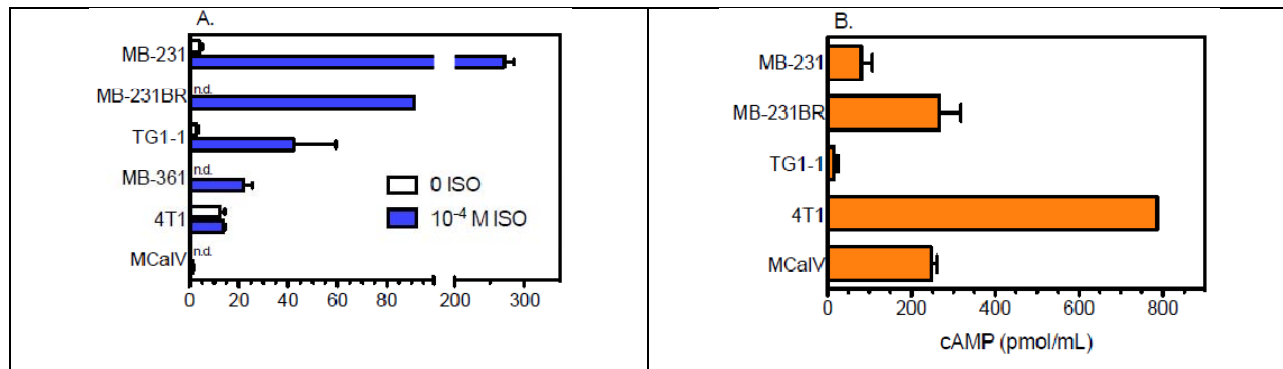


Figure 8. Heterogeneity of cAMP response to β -AR and adenylate cyclase stimulation in breast cancer cell lines. cAMP production was measured after stimulation with (A) 0 ISO or 10⁻⁴ M ISO (5 minutes) or (B) 10⁻⁴ M forskolin (20 minutes). All reactions took place in the presence of 100 μ M IBMX. cAMP was determined by ELISA. Results shown are mean \pm SEM of 1-4 experimental repetitions. n.d. = not detectable; the level of detection is 1 pmol/mL.

production, the kinetics of cAMP production in the two cell lines with the highest β -AR expression, MDA-MB-231 and the brain seeking variant MDA-MB-231BR (Fig. 9). After 60 minutes, cAMP decreased to near baseline in MDA-MB-231BR, but remained elevated in MDA-MB-231. These differences had functional consequences: ISO and the β 2-AR-selective agonist terbutaline increased vascular endothelial

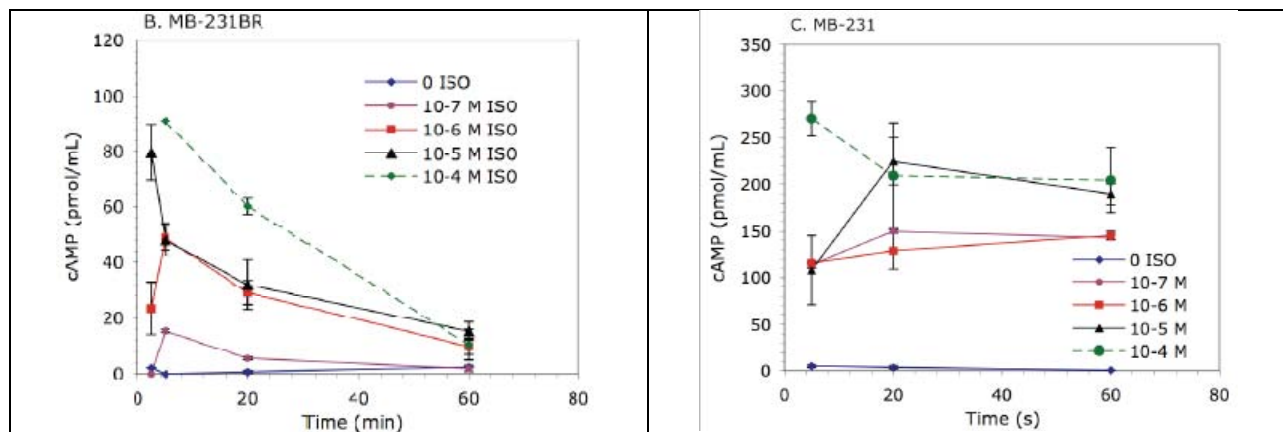


Figure 9. Kinetics of cAMP production with β -AR activation. Varying concentrations of ISO were added to (Left) MDA-MB-231BR, and (Right) MDA-MB-231 in the presence of IBMX for varying periods of time. Intracellular cAMP concentration was determined by ELISA. Results shown are mean \pm SEM of 1-5 experimental repetitions.

growth factor (VEGF) production *in vitro* by MB-231BR, but β -AR stimulation did not alter VEGF production by MB-231 (Fig. 10). Furthermore, β -AR stimulation did not alter MB-231BR or MB-231 proliferation *in vitro* (Not Shown). In summary, therapeutic manipulation of the β -AR-based stress response is a highly promising method to inhibit angiogenesis, but only in those cell lines with the appropriate downstream machinery, as represented here by MDA-MB-231BR. There are many cell lines which will not respond to this therapy (such as MDA-MB-231) and tests of tumor biopsies for candidate tumors cannot settle merely for quantifying receptor number, as some cell lines which do not have functional responses to β -AR signaling (such as MDA-MB-231) have extremely high receptor numbers. This work has been submitted as a manuscript **Madden K, Szpunar M, Brown E. (2009) Heterogeneity of**

β -AR expression, signaling, and function in breast cancer cell lines which is reproduced at the end of this report.

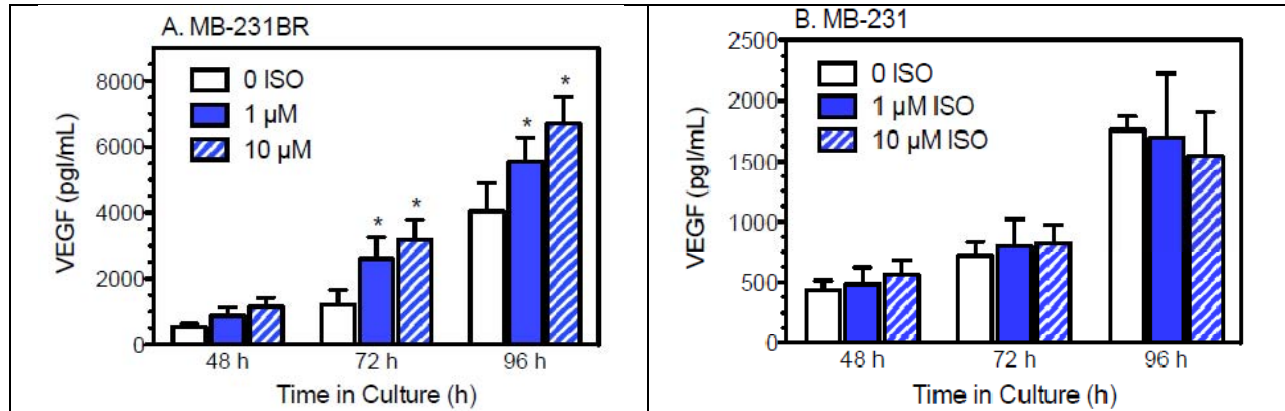


Figure 10. β -AR activation and VEGF production in vitro. ISO at varying doses was added to (A) MB-231BR, and (B) MB-231. Cell-free supernatant was harvested at varying time points, and VEGF content was determined by ELISA, n=3 each. Asterisks indicate statistically significant versus 0 ISO at each time point in culture by Bonferroni post-hoc analysis ($p < 0.05$).

Key Research Accomplishments in the Past Year

- 1) Completed our development of the MPFRAP with flow technique, leading to a publication.
- 2) Applied MP-FRAP to a study of polymer delivery systems, leading to a submitted manuscript.
- 3) Developed significant data implicating macrophages in the ordering of collagen in breast tumors as quantified by Second Harmonic Generation.
- 4) Completed our study of β -AR angiogenic signaling in breast tumor models, leading to a submitted manuscript.

Reportable Outcomes

Over the past year my laboratory has published one paper based upon work funded by this award:

Sullivan K, Sipprell W, Brown E, Brown E. (2009) Improved model for multi-photon fluorescence recovery after photobleaching (MP-FRAP) expands the application of MP-FRAP within the in vivo environment. *Biophysical Journal* 96:5082-5094

I have also continued to advise a graduate student from my old laboratory on technical aspects of MPFRAP, leading to another publication:

Chauhan V, Lanning R, Diop-Frimpong B, Mok W, Brown E, Padera T, Boucher Y, Jain RK. (2009) Multiscale diffusion measurements reveal the cellular and interstitial contributions to molecular hindrance in vivo. *In press, Biophysical Journal*.

Over the past year my laboratory has contributed to the submission for publication of two additional manuscripts based upon work funded by this award:

Madden K, Szpunar M, Brown E. (2009) Heterogeneity of β -AR expression, signaling, and function in breast cancer cell lines. *Manuscript submitted*.

Li J, Sullivan K, Brown E, Anthamatten M. (2009) Thermally activated diffusion in reversibly associating polymers. *Manuscript submitted*.

Over the past year I have also been asked to write two book chapters, which are in preparation:

Sullivan K, Majewska A, Brown E FRAP and Multiphoton FRAP. In: Yuste R, Helmchen F, Konnerth A. (eds). *Imaging in Neuroscience and Development: A Laboratory Manual*. Cold Spring Harbor Laboratory Press, Cold Spring Harbor, New York. In preparation.

Madden K, Majewska A, Brown E A Practical Guide to in vivo Imaging of Tumors. In: Yuste R, Konnerth A. (eds). *Imaging in Neuroscience and Development: A Laboratory Manual*. Cold Spring Harbor Laboratory Press, Cold Spring Harbor, New York. In preparation.

Over the past year I have given four invited talks based upon work funded by this award:

“Epifluorescence Microscopy” Invited Lecture presented at the OSA Rochester Chapter Biomedical Microscopy Shootout, Rochester, NY, 2009

“Second Harmonic Generation (SHG) Imaging of Tumor Biology” Invited lecture presented at the Imaging Science & Technology Rochester Chapter Meeting, Rochester, NY, 2009

“Quantifying collagen organization in breast tumors using Second Harmonic Generation” Invited lecture presented at the National Taiwan University, Taipei, Taiwan, 2009

“Quantifying diffusion in the presence of flow using Multiphoton Fluorescence Recovery After Photobleaching” Invited lecture presented at the National Taiwan University, Taipei, Taiwan, 2009

Over the past year my laboratory contributed to five poster presentations based upon work funded by this award:

Sullivan K, Sipprell III W, Brown E, Brown E Expanding the applicability of the multi-photon fluorescence recovery after photobleaching technique in vivo using a new diffusion-convection model Biophysical Society Annual Conference, 2009

Li, J, Sullivan K, Brown E, Anthamatten M Analysis of Diffusion through Dynamic Network Polymers using Multi-photon Fluorescence Recovery after Photobleaching American Physical Society Annual Meeting, 2009.

Sullivan K, Sipprell III W, Brown E, Brown E Expanding the applicability of the multi-photon fluorescence recovery after photobleaching technique in vivo using a new diffusion-convection model American Physical Society Annual Meeting, 20, 2009

Szpunar M, Madden K, Brown E Heterogeneity of beta-adrenergic receptor (β -AR) signal transduction and vascular endothelial growth factor (VEGF) production by breast cancer cell lines PNIRS, 2009

Madden K, Szpunar M, Brown E Beta-adrenergic receptor (β -AR) signaling differs between the human breast cancer cell line MB-231 and its brain-metastasizing variant MB-231BR PNIRS, 2009

Over the past year, in recognition of my contribution to breast cancer research I was named an Assistant Professor of Oncology

Conclusions

My laboratory is now finishing its fourth year of existence, and its fourth year of funding under this award. We are on pace to produce four publications and two book chapters based upon work from this past year. I feel that significant progress is enabled by the generous support of the Era of Hope Scholar Award.

References

- 1 Mertz, J. & Moreaux, L., Second-harmonic generation by focused excitation of inhomogeneously distributed scatterers. *Opt. Commun.* 196 (1-6), 325-330 (2001).
- 2 Brown, E. *et al.*, Dynamic imaging of collagen and its modulation in tumors in vivo using second-harmonic generation. *Nat Med* 9 (6), 796-800 (2003).
- 3 Sidani, M., Wyckoff, J., Xue, C., Segall, J.E., & Condeelis, J., Probing the microenvironment of mammary tumors using multiphoton microscopy. *J Mammary Gland Biol Neoplasia* 11 (2), 151-163 (2006).
- 4 Wang, W. *et al.*, Single cell behavior in metastatic primary mammary tumors correlated with gene expression patterns revealed by molecular profiling. *Cancer Res* 62 (21), 6278-6288 (2002).
- 5 Condeelis, J. & Segall, J.E., Intravital imaging of cell movement in tumours. *Nat Rev Cancer* 3 (12), 921-930 (2003).
- 6 Provenzano, P.P. *et al.*, Collagen reorganization at the tumor-stromal interface facilitates local invasion. *BMC Med* 4 (1), 38 (2006).
- 7 Parsell, D.A., Mak, J.Y., Amento, E.P., & Unemori, E.N., Relaxin binds to and elicits a response from cells of the human monocytic cell line, THP-1. *J Biol Chem* 271 (44), 27936-27941 (1996).
- 8 Samuel, C.S., Lekgabe, E.D., & Mookerjee, I., The effects of relaxin on extracellular matrix remodeling in health and fibrotic disease. *Adv Exp Med Biol* 612, 88-103 (2007).
- 9 Samuel, C.S., Relaxin: antifibrotic properties and effects in models of disease. *Clin Med Res* 3 (4), 241-249 (2005).
- 10 Binder, C., Hagemann, T., Husen, B., Schulz, M., & Einspanier, A., Relaxin enhances in-vitro invasiveness of breast cancer cell lines by up-regulation of matrix metalloproteases. *Mol Hum Reprod* 8 (9), 789-796 (2002).
- 11 Grouf, J.L., Throm, A.M., Balestrini, J.L., Bush, K.A., & Billiar, K.L., Differential effects of EGF and TGF-beta1 on fibroblast activity in fibrin-based tissue equivalents. *Tissue Eng* 13 (4), 799-807 (2007).
- 12 Ingman, W.V., Wyckoff, J., Gouon-Evans, V., Condeelis, J., & Pollard, J.W., Macrophages promote collagen fibrillogenesis around terminal end buds of the developing mammary gland. *Dev Dyn* 235 (12), 3222-3229 (2006).
- 13 Politis, D., Romano, J., & Wolf, M., *Subsampling*. (Springer, New York, 1999).
- 14 Thaker, P.H. *et al.*, Chronic stress promotes tumor growth and angiogenesis in a mouse model of ovarian carcinoma. *Nat Med* 12 (8), 939-944 (2006).
- 15 Raju, B., Haug, S.R., Ibrahim, S.O., & Heyeraas, K.J., Sympathectomy decreases size and invasiveness of tongue cancer in rats. *Neuroscience* 149 (3), 715-725 (2007).
- 16 Ben-Eliyahu, S., Shakhar, G., Page, G.G., Stefanski, V., & Shakhar, K., Suppression of NK cell activity and of resistance to metastasis by stress: a role for adrenal catecholamines and beta-adrenoceptors. *Neuroimmunomodulation* 8 (3), 154-164 (2000).

Improved Model of Fluorescence Recovery Expands the Application of Multiphoton Fluorescence Recovery after Photobleaching in Vivo

Kelley D. Sullivan,^{†*} William H. Sipprell III,[‡] Edward B. Brown Jr.,[§] and Edward B. Brown III[‡]

[†]Department of Physics and Astronomy, and [‡]Department of Biomedical Engineering, University of Rochester, Rochester, New York; and [§]Department of Physics, Manhattan College, Riverdale, New York

ABSTRACT Multiphoton fluorescence recovery after photobleaching is a well-established microscopy technique used to measure the diffusion of macromolecules in biological systems. We have developed an improved model of the fluorescence recovery that includes the effects of convective flows within a system. We demonstrate the validity of this two-component diffusion-convection model through in vitro experimentation in systems with known diffusion coefficients and known flow speeds, and show that the diffusion-convection model broadens the applicability of the multiphoton fluorescence recovery after photobleaching technique by enabling accurate determination of the diffusion coefficient, even when significant flows are present. Additionally, we find that this model allows for simultaneous measurement of the flow speed in certain regimes. Finally, we demonstrate the effectiveness of the diffusion-convection model in vivo by measuring the diffusion coefficient and flow speed within tumor vessels of 4T1 murine mammary adenocarcinomas implanted in the dorsal skinfold chamber.

INTRODUCTION

Fluorescence recovery after photobleaching (FRAP) was developed in the 1970s as a method to probe the local mobility of macromolecules in living tissue (1–4). Briefly, FRAP is performed by using an intense laser flash to irreversibly photobleach a region of interest within a fluorescent sample and then monitoring the region of interest with the attenuated beam as still-fluorescent molecules from outside the region diffuse inward to replace the bleached molecules. FRAP relies on single-photon excitation of the fluorescent sample, which generates fluorescence throughout the light cone of the objective. Fluorescence and photobleaching are therefore unconfined in three dimensions, generally limiting the technique to thin samples ($\sim 1\ \mu\text{m}$) for measurement of absolute diffusion coefficients. FRAP with spatial Fourier analysis (5,6) allows thicker samples to be investigated; however, deep-tissue imaging is still prohibited due to the poor depth penetration of epifluorescence microscopy. The FRAP technique was significantly enhanced with the advance to multiphoton excitation. The intrinsic spatial confinement of multiphoton excitation (7) allows multiphoton fluorescence recovery after photobleaching (MP-FRAP) to be performed within thick samples, while the greater depth penetration of multiphoton imaging (8) allows MP-FRAP to be performed deep within scattering samples (9).

The existing mathematical theory of MP-FRAP assumes that diffusion is the only recovery mechanism and so does not account for the possibility of convective flow within the focal volume, a situation that is now likely to arise as MP-FRAP is applied to a greater variety of in vivo applications. The presence of an unexpected significant convective

flow in an MP-FRAP experiment can produce erroneously high diffusion coefficients when the existing diffusion-only model is used to analyze the data. It is important, therefore, to include convective flow in the MP-FRAP derivation and to determine over what range of flow speeds the MP-FRAP technique can thereby provide accurate diffusion coefficients.

We expect this new diffusion-convection model to be crucial for diffusion studies conducted in tissues with above-average interstitial flow. Kidney studies, for example, are already enjoying advances due to the application of multiphoton imaging techniques (10–12). Interstitial flow within the juxtaglomerular apparatus of the kidney has been measured via multiphoton video imaging to be $27.9 \pm 7.2\ \mu\text{m/s}$ (13), which is a significant enough flow speed to elicit erroneous diffusion coefficients when measured via MP-FRAP and fit to the diffusion-only model. MP-FRAP with the new derivation may also find a place in the burgeoning world of microfluidics, where measurements of diffusion coefficients (and flow speeds) are already in demand (14–16).

Through application of the Stokes-Einstein relation, the diffusion coefficient obtained from MP-FRAP measurements can be used to calculate fluid viscosity. In a healthy human, blood plasma viscosity maintains a narrow range of values, 1.10–1.30 mPas at 37°C (17). An elevated plasma viscosity, in the extreme case (greater than twice the normal value) known as hyperviscosity syndrome (18), is indicative of many disease states. For example, a positive correlation has been found between the degree of plasma viscosity elevation and the severity of coronary heart disease (19), as well as the incidence of heart attack or stroke (20–22). Hyperviscosity is often associated with Waldenström's macroglobulinemia and multiple myeloma (23). Elevated plasma viscosity has been indicated in cancer development, particularly among the gynecologic cancers (24). Plasma

Submitted August 22, 2008, and accepted for publication April 3, 2009.

*Correspondence: ksullivan@pas.rochester.edu

Editor: George Barisas.

© 2009 by the Biophysical Society
0006-3495/09/06/5082/13 \$2.00

doi: 10.1016/j.bpj.2009.04.020

viscosity can also be used to assess changes in acute phase response due to trauma (17,25). MP-FRAP offers a noninvasive, real-time measure of plasma viscosity, which could be used to probe more deeply the connection between plasma viscosity and these (and other) disease states and/or the response of these disease states to treatments. However, our results show that measurement of the diffusion coefficient, and therefore plasma viscosity, in blood vessels requires the use of our diffusion-convection model for accurate fitting of MP-FRAP recovery curves under the influence of significant directed flow.

A fortunate benefit of the new derivation is that for a relatively wide range of diffusion coefficients and flow speeds, both parameters can be measured accurately. Other techniques have addressed the possibility of combined convective flow and diffusive transport. Axelrod et. al. (2) derived a diffusion-convection model similar to the one presented here, but for conventional (one-photon) FRAP. Later researchers utilized FRAP with Fourier analysis, which uses a video-based analysis of photobleaching recovery data to measure flow speeds and offer insight into flow directions (26–28). Fluorescence correlation spectroscopy is also capable of measuring flow speeds (29), while single particle tracking offers a true velocity vector (30,31).

As discussed, however, single-photon excitation techniques fail to offer the combined spatial resolution and depth penetration of MP-FRAP. Other techniques offering similar spatial resolution as MP-FRAP include multiphoton fluorescence correlation spectroscopy (32,33) and the closely related two-photon image correlation spectroscopy (ICS) (34). Both of these techniques are capable of measuring flow velocities, as well as diffusion, and two relatively new variations of image correlation spectroscopy, k-space ICS (35), and spatio-temporal ICS (36), explicitly offer the ability to measure diffusion coefficients and velocity vectors simultaneously. However, the need of the various correlation spectroscopies for both low concentrations of fluorophores and low background noise, compared with the need of FRAP techniques for high concentrations of fluorophores and subsequent resistance to background noise, means that the correlation spectroscopies and the photobleaching recovery techniques are complementary, not competitive.

In this article, we will first derive the theory of MP-FRAP with both diffusion and convection. Then, we will use computer-generated data to understand how MP-FRAP curves evolve under flow and to predict how the diffusion-only and diffusion-convection MP-FRAP models will fit data with convective flow. Next, we will perform MP-FRAP experimentally using tracers with known diffusion coefficients in situations with known flow speed, and determine specific cutoff speeds that define regimes where the diffusion-only and diffusion-convection models produce accurate diffusion coefficients (and/or flow speeds). Lastly, we will apply the diffusion-convection model in vivo under a range of flow conditions.

THEORY

In the existing MP-FRAP model, diffusion is assumed to be the only mechanism for recovery. The diffusive recovery after a brief bleaching pulse is given by Brown et. al (37),

$$F(t) = F_0 \sum_{n=0}^{\infty} \frac{(-\beta)^n}{n!} \times \frac{1}{(1+n+2nt/\tau_D)} \frac{1}{(1+n+2nt/R\tau_D)^{1/2}}, \quad (1)$$

where β is the bleach depth parameter, τ_D is the characteristic diffusion time, and R is the square of the ratio of the axial to the radial dimensions of the focal volume. The diffusion coefficient is given by $D = \omega_r^2/8\tau_D$, where ω_r is the radial $1/e^2$ radius of the two-photon focal volume. With only two fitting parameters, β and τ_D , fits to the fluorescence recovery using the existing model are very robust. In the absence of flow, a three-to-four decade range of seed values for the fitting parameters required by the fitting program will produce convergence to the same, low-residual, fit.

By adding a time-dependent coordinate shift to the standard model of diffusive recovery before its convolution with the excitation laser profile (see Appendix), we arrive at an improved diffusion-convection model that describes fluorescence recovery in the presence of convective flow, as well as diffusion:

$$F(t) = F_0 \sum_{n=0}^{\infty} \frac{(-\beta)^n}{n!} \times \frac{\exp\left[-\frac{4nt^2(1/\tau_{v_x}^2 + 1/\tau_{v_y}^2)}{1+n+2nt/\tau_D}\right] \exp\left[-\frac{4nt^2/\tau_{v_z}^2}{1+n+2nt/R\tau_D}\right]}{(1+n+2nt/\tau_D)(1+n+2nt/R\tau_D)^{1/2}}. \quad (2)$$

In this model, an additional fitting parameter, τ_v , is introduced, which describes the characteristic recovery time due to convective flow. For one-dimensional flow parallel to the imaging plane, this equation reduces to

$$F(t) = F_0 \sum_{n=0}^{\infty} \frac{(-\beta)^n}{n!} \times \frac{\exp\left[-\frac{4n(t/\tau_v)^2}{1+n+2nt/\tau_D}\right]}{(1+n+2nt/\tau_D)(1+n+2nt/R\tau_D)^{1/2}}. \quad (3)$$

The flow speed is easily calculated as $v = \omega_r/\tau_v$. This form of the equation readily reduces to that derived by Axelrod et. al. (2) for thin samples with flow measured via one-photon FRAP if the intensity profile is assumed to be two-dimensional (square-root term in denominator disappears). For the purpose of this article, we will focus on the one-dimensional diffusion-convection form (Eq. 3), unless explicitly stated otherwise. This formula produces MP-FRAP recovery

curves that are indistinguishable from MP-FRAP recovery curves derived using the diffusion-only formula (Eq. 1) when flow speeds are extremely low. Increasing the flow speed shortens the recovery time and alters the shape of the MP-FRAP recovery curves, eventually producing curves that approach an almost sigmoidal shape at high flow speeds (see Fig. 1).

With the improved diffusion-convection model, we can now measure diffusion accurately in the presence of flow while simultaneously measuring the flow speed. However, the introduction of a third fitting parameter complicates the fit. We might now expect that when either diffusion or flow dominates the fluorescence recovery, the fitting program will yield inaccurate values for the nondominant parameter. Care must be taken to define the range of flow speeds over which the diffusion coefficient and flow speed may be measured accurately.

METHODS

Computer-generated data and fitting

Fluorescence recovery curves were generated using the diffusion-convection model and fit to both the diffusion-only and diffusion-convection models using the `lsqcurvefit` function in MATLAB (The MathWorks, Natick, MA). We added Poisson-distributed noise to the generated data in proportion to the relative noise expected for either *in vitro* (3%) or *in vivo* (5%) experiments, as determined from previous experience (37). Three experimentally relevant bleach depths were also chosen: 0.2, 0.6, and 1.0 (37). For each bleach depth/noise combination, a range of diffusion coefficients and flow speeds was explored. After fitting the recovery curves, the ratio of fit diffusion coefficient to input diffusion coefficient (with both the diffusion-only and diffusion-convection models) and the ratio of fit speed to input speed (with the diffusion-convection model) were plotted versus input speed. Initial seed values for the fitting parameters required as inputs to the `lsqcurvefit` function were generated via algorithms developed from limits

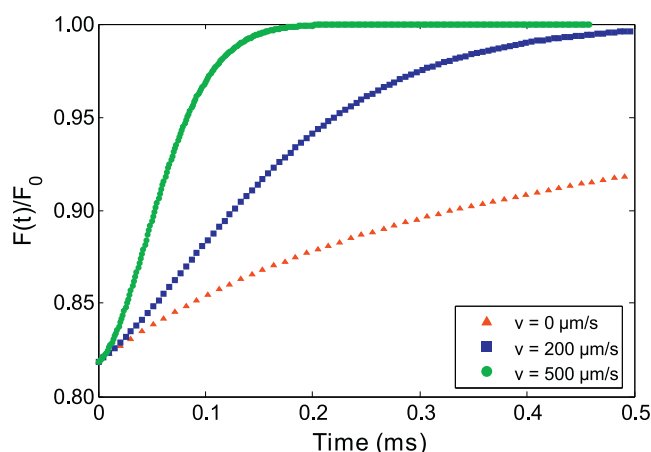


FIGURE 1 Comparison of the recovery of computer-generated MP-FRAP curves for a macromolecule with $D = 9.2 \mu\text{m}^2/\text{s}$ and differing values of flow speed. The lower curve is a diffusion-only recovery ($v = 0 \mu\text{m/s}$), while the middle recovery curve has a moderate amount of flow ($v = 120 \mu\text{m/s}$), and the upper recovery curve is flow-dominated ($v = 500 \mu\text{m/s}$). The shape of the curve changes as flow increases, eventually leading to an almost sigmoidal shape for the flow-dominated recovery.

to the diffusion-convection model equation and assumed no a priori knowledge of the experimental system or of the particular diffusion coefficients and flow speeds. Specifically, the formula used to calculate a seed value for β was derived by solving the recovery equation (Eq. 3) at $t = 0$ for β in terms of $F(0)/F_0$, plotting a range of bleach depth parameters as a function of $F(0)/F_0$, and then choosing the best-fit polynomial to the curve. Seed values for τ_D were easily estimated as the one-half recovery time of the MP-FRAP recovery curve ($\tau_{1/2}$). And the seed value for flow speed was approximated as $v = (x_{1/2})^{1/2}(\omega_r/\tau_{1/2})$, where $x_{1/2}$ was determined by taking the limit of the recovery equation as $\tau_D \rightarrow \infty$, then plotting $F(x)/F_0$, with $x = (vt/\omega_r)^2$, and finally picking the value at which $F(x)/F_0$ was half recovered.

Experimental apparatus

Laser light was generated by a tunable, mode-locked Ti:Sapphire laser (Mai Tai; Spectra Physics, Mountain View, CA), yielding 80-fs pulses at a repetition rate of 100 MHz. Rapid modulation of the laser power to produce monitor and bleach intensities was provided by a KDP* Pockels Cell (model No. 350-80; Conoptics, Danbury, CT). Timing of the bleach and monitor pulses was delivered by a pulse generator (model No. DG535, Stanford Research Systems, Sunnyvale, CA), while the voltage output to the Pockels Cell was set and switched by a specially designed control box. The output of the Pockels Cell was directed through an Olympus Fluoview 300 laser-scanning microscope to the back aperture of the objective lens (0.8 NA, 40 \times water immersion; Olympus, Center Valley, PA). Proper overfilling of the back aperture of the objective lens was achieved for all experiments (see PSF Calibration below). Overfilling is accomplished when the $1/e$ radius of the laser beam is greater than or equal to the radius of the back aperture of the lens. The objective lens focused the excitation beam within the fluorescent sample (Fig. 2). The fluorescence emission was separated from the excitation light by a short-pass dichroic mirror (model No. 670 DCSX-2P, Chroma Technologies, Brattleboro, VT). For the *in vitro* experiments, emission signals were further separated by a second dichroic mirror and each was detected by a photomultiplier tube (PMT) (Hamamatsu, Bridgewater, NJ). The output from the PMT monitoring the green channel (fluorescent dye; see *in vitro* MP-FRAP below) could be directed to a photon counter (model No. SR400; Stanford Research Systems, Sunnyvale, CA), for general inquiry into the fluorescence behavior, or to a multichannel scaler/averager

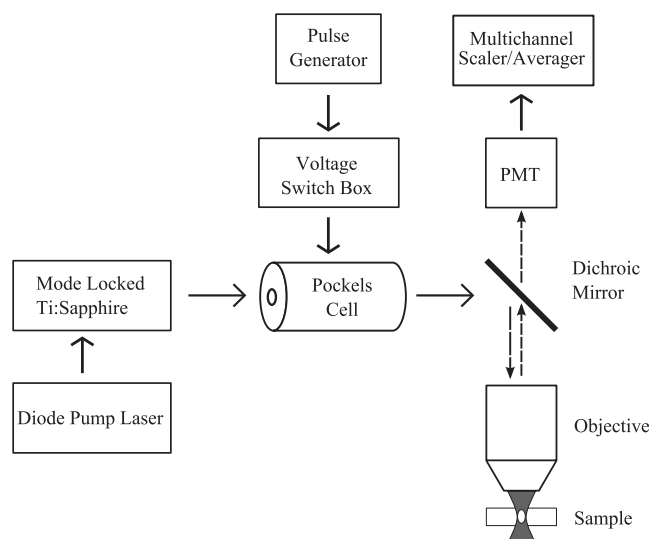


FIGURE 2 Equipment diagram of MP-FRAP apparatus. To obtain line-scan images for flow speed comparison, a laser scanning system was included in the system. For *in vitro* experiments, an additional dichroic mirror and PMT were added to separate and measure the red fluorescence of the polystyrene beads.

(model No. SR430; Stanford Research Systems), for fluorescence recovery data collection. Output from the PMT monitoring the red channel (fluorescent microspheres; see *In vitro* MP-FRAP below) was directed to the Olympus imaging software. For increased throughput, data collection was largely automated via LabVIEW (National Instruments, Austin, TX).

PSF calibration

The $1/e^2$ radial and axial dimensions of the two-photon excitation volume were verified by scanning the excitation volume across subresolution fixed fluorescent beads (Molecular Probes/Invitrogen, Eugene, OR). For the radial dimension, xy scans were taken and the intensity profiles of the beads were measured using ImageJ (National Institutes of Health, Bethesda, MD). For the axial dimension, z -stack images were acquired, then the intensity profiles of the beads in each image in the stack analyzed in ImageJ to determine the peaks of the intensity profiles and the peak values plotted versus image depth to build intensity profiles in the axial direction. The results of both measurements were compared against theoretical values. For this work, we defined the $1/e^2$ radii of the focal volume to be $0.403\ \mu\text{m}$ in the radial direction and $2.22\ \mu\text{m}$ in the axial direction for a 0.8 NA objective, properly overfilled with 780-nm laser light.

In vitro MP-FRAP

For *in vitro* testing of the flow model, fluorescent samples were produced by mixing fluorescein isothiocyanate (FITC) conjugated to bovine serum albumin (BSA) or 2000 kDa dextran (dextran) (Molecular Probes/Invitrogen) diluted to 1 mg/mL in phosphate buffered saline (PBS) with 1 $\mu\text{L}/\text{mL}$ red fluorescent microspheres (FluoSpheres; Molecular Probes/Invitrogen). The solution was suspended in a syringe and allowed to flow freely through a thin tube (0.28 mm radius) and into a channel, capped by a No. 1.5 coverslip and immersed in a pool filled with PBS. The rate of flow was set by adjusting the height of the syringe relative to the channel. For MP-FRAP measurements, the excitation focal volume was kept stationary within the flowing solution in the channel, and the excitation intensity rapidly modulated between a strong bleaching pulse and a weak monitoring pulse. For independent flow speed measurements, the excitation volume was scanned repeatedly along a one-dimensional line parallel to the fluid flow at constant excitation intensity, thus producing a line-scan image with dimensions of position versus time (38). The angle of the sporadic streaks in the line-scan image, representing the movement of the microspheres, was used to calculate the flow speed.

In vivo tumor blood vessel imaging

4T1 murine mammary adenocarcinoma cells (American Type Culture Collection, Manassas, VA) were injected ($\sim 4 \times 10^6$ in 50 μL) into the inguinal mammary fat pad of 6–8-week-old female BALB/cByJ mice (Jackson Laboratory, Bar Harbor, ME). Tumors were removed for implant into dorsal skinfold chambers when they reached ~ 2.5 mm in diameter.

Male BALB/cByJ mice (Jackson Laboratory) were anesthetized by intraperitoneal injection of a mixture of 90 mg/kg ketamine (IVX Animal Health, St. Joseph, MO) and 9 mg/kg xylazine (Hospira, Lake Forest, IL), and outfitted with a titanium dorsal skinfold chamber as previously described (39). Two days later, a small fragment of 4T1 tumor (~ 0.5 mm) was placed in the window of the chamber and allowed to grow for one week before imaging.

Animals containing tumors growing in the dorsal skinfold chamber were anesthetized with ketamine/xylazine, as described above. FITC-dextran was injected intravenously (0.2 mL at 10 mg/mL in PBS), and animals were positioned under the microscope objective lens. MP-FRAP was performed as described above, with the focal volume positioned in the center of the vessel in the xy plane, but largely within the red blood cell-free region along the z axis to maximize fluorescent signal. Line-scans were also performed as described, using the shadows of RBCs, which do not take up FITC-dextran, instead of fluorescent beads.

All animal care and use was in accordance with the policies of the University of Rochester Committee on Animal Resources.

Data analysis

As with the computer-generated data, experimental MP-FRAP recovery curves were fit to the diffusion-only and diffusion-convection models using the MATLAB `lsqcurvefit` function, which is based on the Levenberg-Marquardt algorithm. Line-scan images were analyzed using ImageJ software.

RESULTS

In silico: testing the limits of the MP-FRAP models

We used computer-generated data to explore the effect of convective flow on the shape and speed of fluorescence recovery, and to probe the conditions (input recovery parameters, noise, focal volume) under which the MATLAB fitting algorithm could correctly recover the diffusion coefficient, assuming the diffusion-convection model is physically accurate (which is tested in *In Vitro* MP-FRAP). Conditions under which the diffusion-only model produces accurate diffusion coefficients were assessed by generating fluorescence recovery curves using the diffusion-convection model and fitting them to the diffusion-only model, then comparing the input diffusion coefficients and fit diffusion coefficients. Beginning with a combination of a relative noise of 3% and a bleach-depth parameter of 0.6, we generated curves for a series of diffusion coefficients ranging from 0.5 to 500 $\mu\text{m}^2/\text{s}$ over a range of flow speeds from 0.1 to 10,000 $\mu\text{m}/\text{s}$. Fig. 3

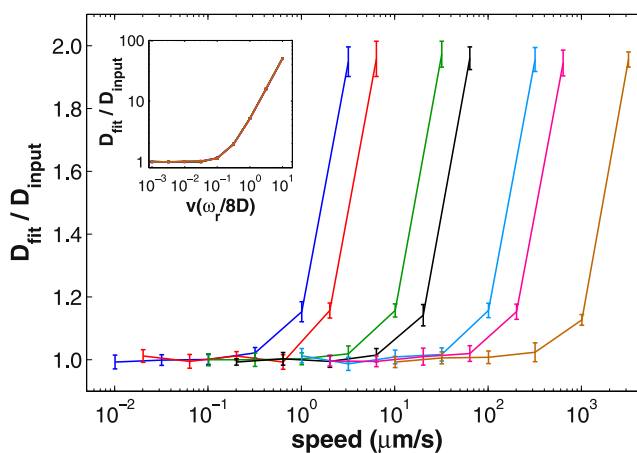


FIGURE 3 Conditions for accurate fitting using the diffusion-only model, as assessed by fitting computer-generated data. Fluorescence recovery curves were generated with the diffusion-convection model, keeping the bleach depth parameter and relative noise constant at 0.6 and 3%, respectively, while exploring a range of speeds (plotted logarithmically) for each of a set of diffusion coefficients (left to right: $D = 0.5, 1, 5, 10, 50, 100, 500\ \mu\text{m}^2/\text{s}$). The data were fit to the diffusion-only model, and the diffusion coefficients produced were normalized to the associated input diffusion coefficients. Hence, an accurate result produces a ratio of one. As the input speed increases beyond a certain cutoff value, the diffusion-only model yields a growing overestimate to the diffusion coefficient. By scaling the input speed along the horizontal axis (*inset*), the curves for each value of the diffusion coefficient overlay onto a single curve.

shows that for this series of diffusion coefficients, the diffusion-only model begins yielding erroneously high diffusion coefficients as the flow speed increases, and that the error in determining the diffusion coefficient commences at flow speeds that vary with the diffusion coefficient of the tracer in question. By scaling the speed along the horizontal axis (*inset*), such that $v_s = v(\omega_r/8D)$, the curves for each value of the diffusion coefficient overlay onto one curve, and a universal behavior can be observed: the diffusion-only model produces erroneous diffusion coefficients ($D_{\text{fit}}/D_{\text{input}} \gg 1$) as the scaled speed approaches $v_s \sim 0.3$. This scaling behavior allowed us to complete our investigations of the remaining noise/bleach depth parameter combinations using only the diffusion coefficients representative of BSA and dextran, the two tracer molecules used in our *in vitro* experiments. With all combinations of noise and bleach-depth evaluated (3% and 5% relative noise, and β of 0.2, 0.6, 1.0), we find that the behavior of the $D_{\text{fit}}/D_{\text{input}}$ curve is unchanged (data not shown). The behavior of the $D_{\text{fit}}/D_{\text{input}}$ curve also remained unchanged when a significantly larger focal volume was assumed, $\omega_r = 0.646 \mu\text{m}$ and $\omega_z = 5.81 \mu\text{m}$, corresponding to a numerical aperture of 0.5 (data not shown).

To evaluate the conditions under which the diffusion-convection model produces accurate diffusion coefficients, we generated, and fit, fluorescence recovery curves using the diffusion-convection model for diffusion coefficients representing BSA and dextran over a range of flow speeds. We show representative results in Fig. 4 *a* for $\beta = 0.6$ and relative noise = 3%, where the ratio of fit diffusion coefficient to input diffusion coefficient is displayed along with the ratio of fit speed to input speed. Of greatest importance to note is that the diffusion-convection model produces accurate values for the diffusion coefficient for values of flow speed much greater than those for which the diffusion-only model produces accurate values for the diffusion coefficient. We also note that at the extremes of the plot, representing results from fits to fluorescence recoveries dominated by either diffusion (on the left) or flow (on the right), the fit accurately determines the dominant parameter (i.e., a ratio of one with a small standard deviation), while poorly determining the nondominant parameter (i.e., a ratio not equal to one and/or a large standard deviation). For a wide range of scaled speeds, the effects of diffusion and flow on the fluorescence recovery dynamics are reasonably balanced, and both the diffusion coefficient and the flow speed are accurately determined. Based on this result, we can define three regimes: 1) diffusion-dominated, in which only the diffusion coefficient is accurately determined; 2) balanced, in which both the diffusion coefficient and flow speed are accurately determined; and 3) flow-dominated, in which only the flow speed is accurately determined. After completing investigations of the full collection of bleach-depth/noise combinations, we find that the balanced regime, where both the diffusion coefficient and flow speed are well determined, is narrowed as β decreases and/or the relative noise increases

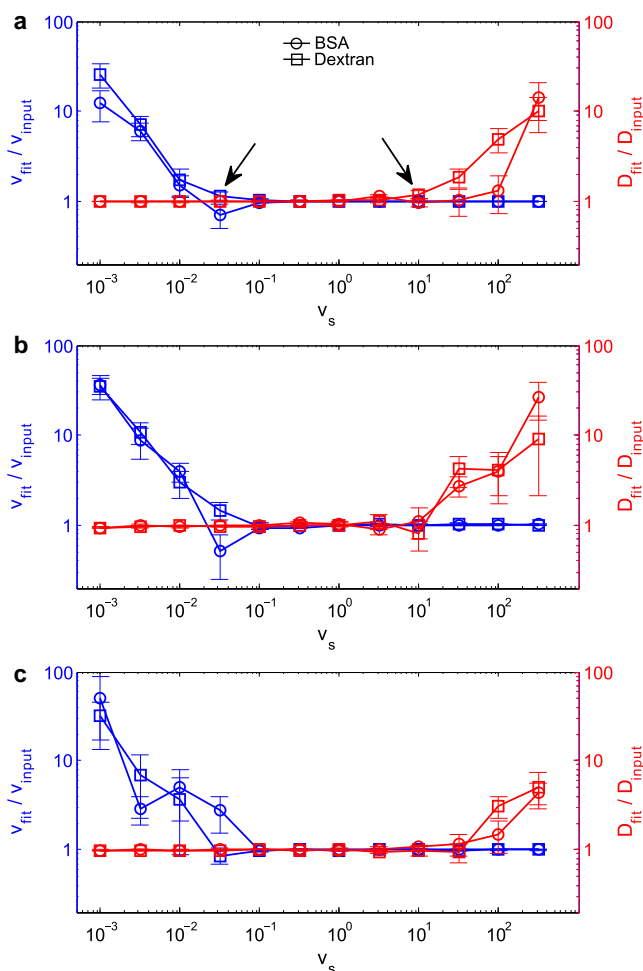


FIGURE 4 Conditions for accurate fitting using the diffusion-convection model, as assessed by fitting computer-generated data. Fluorescence recovery curves were generated with the diffusion-convection model, keeping the bleach-depth parameter and noise level constant while exploring a range of flow speeds (plotted logarithmically) for each of two diffusion coefficients representing BSA and 2000 kDa dextran. The data were fit to the diffusion-convection model, and the diffusion coefficients (red) and flow speeds (blue) produced by the fits were normalized to associated input values. Hence, an accurate result produces a ratio of one. In the case that either diffusion or flow dominates the recovery, the fit poorly determines the nondominant parameter. For a wide range of balanced recoveries, both diffusion and flow are well determined. (a) $\beta = 0.6$ and $N/S = 3\%$, experimentally representative values. Arrows point to regimes where the standard deviations in the nondominant parameter are high, even though the average normalized value is close to one. (b) $\beta = 0.6$ and $N/S = 5\%$; the increase in noise narrows the balanced regime. (c) $\beta = 1.0$ and $N/S = 3\%$; the deeper bleach depth widens the balanced regime.

(Fig. 4 *b*) and is broadened as β increases and/or as the relative noise decreases (Fig. 4 *c*). No change is seen, however, when a larger focal volume is assumed (data not shown). We also find that as we move into either of the two regimes where one parameter dominates the other, the standard deviation in the measurement of the nondominant parameter increases precipitously. This increase in the standard deviation of the nondominant parameter is more sensitive to the scaled speed than are changes in the mean value of $D_{\text{fit}}/D_{\text{input}}$

or $v_{\text{fit}}/v_{\text{input}}$, and therefore, the standard deviation is a more conservative indicator of inaccurate results. The arrows in Fig. 4 *a* point to regimes where the standard deviation in the relevant ratio grows significantly, even while the average of the ratio remains close to one. In Fig. 3, however, we see that using the diffusion-only model to fit data whose recovery is dominated by flow does not produce large standard deviations. This is because the fitting routine must erroneously assign all of the recovery kinetics to diffusion, thus producing a very precise, but very inaccurate, diffusion coefficient. It is only when the diffusion-convection model is used to determine D (and v) that the standard deviations can grow large while the ratio of $D_{\text{fit}}/D_{\text{input}}$ (or $v_{\text{fit}}/v_{\text{input}}$) remains close to one. This is because as the bulk of the recovery is assigned to the dominant parameter and the negligible contribution from the nondominant parameter can fluctuate.

By producing fits to computer-generated data, we have gained important knowledge of the scaling behavior of recovery curves influenced by diffusion and convection. Verifying the diffusion-convection model in subsequent in vitro tests could require, in principle, hundreds of combinations of flow speeds and tracer molecules. However, by taking advantage of the scaling behavior depicted in Fig. 3, we can demonstrate the physical accuracy of the diffusion-convection model using just two tracer molecules and a moderate range of flow speeds. We also determined a range of conditions (recovery parameters, noise, focal volume) over which we can expect to recover accurate diffusion coefficients when fitting experimental curves with the diffusion-convection model, as well as developed expectations for the behavior of our data statistics. For example, we predict that the error in recovering the diffusion coefficient using both the diffusion-only and diffusion-convection models will increase with increasing flow speed, while for some range of low flow speeds both models will produce accurate diffusion coefficients. We also predict that there will be a range of flow speeds over which the diffusion-convection model produces accurate diffusion coefficients and flow speeds, and a range of flow speeds over which the diffusion-convection model produces only accurate flow speeds. Further, we predict that, using the diffusion-convection model, the standard deviation of the nondominant parameter will increase before the average ratio of $D_{\text{fit}}/D_{\text{input}}$ or $v_{\text{fit}}/v_{\text{input}}$ begins to deviate from one, while the diffusion-only model, lacking a nondominant parameter, will produce very precise, but very inaccurate, values of D as flow increases.

In vitro MP-FRAP

For a direct measure of the conditions necessary to yield accurate fits to the diffusion coefficient using the two models, as well as for verification of the physical accuracy of the new diffusion-convection model, we designed an experimental system with known diffusion and known directed flow. FITC-BSA and FITC-dextran were used as

fluorescent tracer molecules. The dramatic difference in molecular weight, 64 kDa and 2000 kDa for BSA and dextran, respectively, was necessary to access the widest range of relevant scaled speeds as suggested by the results of fitting computer-generated data. To determine accuracy of fit, the fit diffusion coefficient was compared against the diffusion coefficient for a diffusion-only system, i.e., performed without experimental flow and fit to the diffusion-only model, and the fit speed was compared against the speed obtained from line-scan data taken concurrently with the MP-FRAP measurements. In the literature, diffusion-coefficient values for BSA vary from 55 to 62 $\mu\text{m}^2/\text{s}$ (6,27,40–43), while values for dextran range from 8.4 to 9.1 $\mu\text{m}^2/\text{s}$ (42,43), when adjusted to 20°C via the Stokes-Einstein relation. Our diffusion-only measurements yielded $52 \pm 0.7 \mu\text{m}^2/\text{s}$ and $9.2 \pm 0.05 \mu\text{m}^2/\text{s}$ for BSA and dextran, respectively, consistent with the literature.

The results of our measurements with flow are summarized in Figs. 5 and 6. Fig. 5 compares results of the accuracy of the diffusion coefficient as given by both the diffusion-only (circles) and diffusion-convection (diamonds) models for the same collection of data. As predicted from fits to the computer-generated data, the standard deviation in the results from experimental data fit by the diffusion-only model does not increase, even as the error becomes great (i.e., $D_{\text{fit}}/D_{\text{input}} \gg 1$). To determine a cutoff speed beyond which the diffusion-only model no longer produces an accurate diffusion coefficient, we define an inaccurate fit by the diffusion-only model as one in which D_{fit}/D_0 is statistically greater

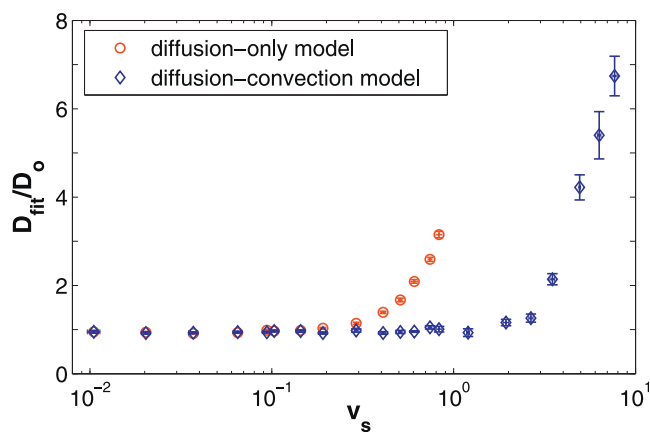


FIGURE 5 Comparison of in vitro experimental data with flow, fit to the diffusion-only and diffusion-convection models. A series of experimental fluorescence recovery curves for FITC-BSA and FITC-2000 kDa dextran were taken over a wide range of known flow speeds (plotted logarithmically). The curves were then fit to both the diffusion-only (circles) and the diffusion-convection (diamonds) models, and the diffusion coefficients produced by each fit were normalized to the value measured in a system without flow and fit to the diffusion-only model. Hence, an accurate result produces a ratio of one. As the flow speed grows beyond $v_s \approx 0.3$, the diffusion-only model yields an increasing overestimate to the diffusion coefficient. The improved diffusion-convection model, however, continues to provide accurate diffusion coefficients for scaled speeds up to $v_s \approx 3$, ~10 times larger than the cutoff speed for the diffusion-only model.

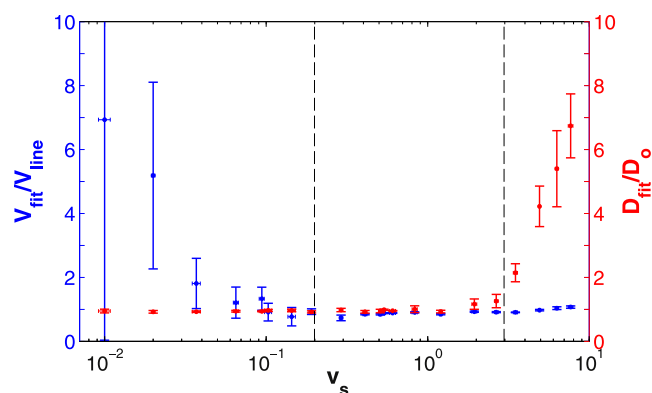


FIGURE 6 Results of fitting in vitro experimental data with flow to the diffusion-convection model. A series of experimental fluorescence recovery curves for FITC-BSA and FITC-2000 kDa dextran were taken over a wide range of known flow speeds (plotted logarithmically). The diffusion coefficients (red) taken from the respective fits to the diffusion-convection model are presented here as ratios with respect to the associated diffusion coefficient measured in a system without flow and fit to the diffusion-only model. The flow speeds (blue) taken from the fits are presented as ratios with respect to flow speeds measured via line-scans. An accurate result produces a ratio of one. As with the computer-generated data, when either diffusion or flow dominates the fluorescence recovery, the fit correctly determines the dominant parameter, but poorly determines the nondominant parameter. For a wide range of balanced recoveries, $0.2 \leq v_s \leq 3$, both parameters are determined accurately. Dotted lines delineate the two experimentally determined cutoff speeds that define the parameter spaces in which the diffusion-convection model accurately determines one (or both) parameters.

than 1.2 (determined by a one-sided hypothesis test), and we see that the diffusion-only model begins yielding inaccurate fits to the diffusion coefficient at a cutoff value of $v_s \approx 0.3$. The diffusion-convection model, meanwhile, continues to provide accurate values for the diffusion coefficient for significantly greater flow speeds.

Fig. 6 displays the accuracy of the results for both the diffusion coefficient and the flow speed as determined by fitting data with the diffusion-convection model. For the diffusion-convection model, our fits to computer-generated data indicated that the standard deviation in fit values of the nondominant parameter can increase before deviations from one arise in the ratio of D_{fit}/D_o or $v_{\text{fit}}/v_{\text{linescan}}$. We therefore define a poor measurement as having a standard deviation $>15\%$ of the mean value. Using this criterion, we can expect the transition from diffusion-dominated to a balanced recovery to occur at $v_s \approx 0.2$ and the transition from balanced to a flow-dominated recovery to occur at $v_s \approx 3$. These experimentally determined cutoff speeds are valid for $\beta \approx 0.5$ and relative noise $\approx 4\%$, chosen to match typical experimental values (37). While our fits to generated data have shown that differing amounts of noise and bleach-depth will shift these cutoff values slightly (see Fig. 4), we can use these cutoff values as estimates of the range of behaviors expected for in vivo experiments.

We also tested the ability of the diffusion-convection model to measure diffusion in the presence of flow in the

axial direction (perpendicular to the imaging plane). With this geometry, it was not feasible to measure flow speeds via line-scans for independent verification. However, by choosing a reservoir height corresponding to a relatively modest flow, we produced a diffusion coefficient for FITC-BSA of $51 \pm 2 \mu\text{m}^2/\text{s}$ ($v_s = 0.9 \pm 0.2$ based on velocity values taken from the fit), which matched our same-day measurement of diffusion in a flow-free system, $D = 53 \pm 4 \mu\text{m}^2/\text{s}$ ($p = 0.42$, $N = 5$). In addition, for a relatively high rate of flow, we found $D = 59 \pm 2 \mu\text{m}^2/\text{s}$ ($v_s = 4 \pm 0.5$), which was statistically larger than the flow-free measurement ($p = 0.0042$, $N = 5$). These results compare well with those derived from measurements taken within the imaging plane.

In vivo MP-FRAP

We chose to demonstrate the effectiveness of the diffusion-convection model in vivo by measuring diffusion (and convection) within living tumor vessels. This model was selected because blood flow through tumor vessels exhibits a wide range of flow speeds with which to fully test the diffusion-convection model in vivo in analogy with our in vitro experimentation. Moreover, measurement of plasma viscosity (using a simple conversion via the Stokes-Einstein equation) has important applications in the study of several disease states. By choosing vessels parallel to the plane of imaging, we could continue to employ the line-scan technique to measure the red blood cell (RBC) speed, which was used as an independent in vivo measurement of transverse flow to compare with our MP-FRAP flow speed measurements. Fig. 7 shows representative recovery curves and associated fits to the diffusion-convection model for FITC-dextran flowing in three different tumor vessels. Table 1 shows the results of fitting the curves to both the diffusion-only and diffusion-convection models, as well as the average RBC speed in that part of the vessel. We have also tabulated the value of the predicted flow scaled speed, v_s , as calculated from RBC speeds and in vitro diffusion coefficient measurements (adjusted to 37°C and $\eta = 1.2$ cP, the viscosity of plasma (44), via the Stokes-Einstein relation). Please note that the data presented for v_s and v_{RBC} represent the mean and standard error of five measurements, while the data presented for $D_{\text{diff-only}}$, $D_{\text{diff-conv}}$, and $v_{\text{diff-conv}}$ represent the fit values from each of three single data curves and the associated error in the fitted parameters. The presence of pulsatile flow caused flow rates to vary within individual vessels, and particularly widely in larger vessels, thus preventing the calculation of meaningful means and standard deviations for speed values. (In this case, the mean and standard deviation would describe the variation in the speed, not the variation in the ability of the diffusion-convection model to fit the data accurately.)

In vessel 1, we see that the RBC speed was $14 \pm 3 \mu\text{m}/\text{s}$, producing a predicted scaled speed of 0.08 ± 0.02 , well below the estimated cutoff speed for accurate fitting with

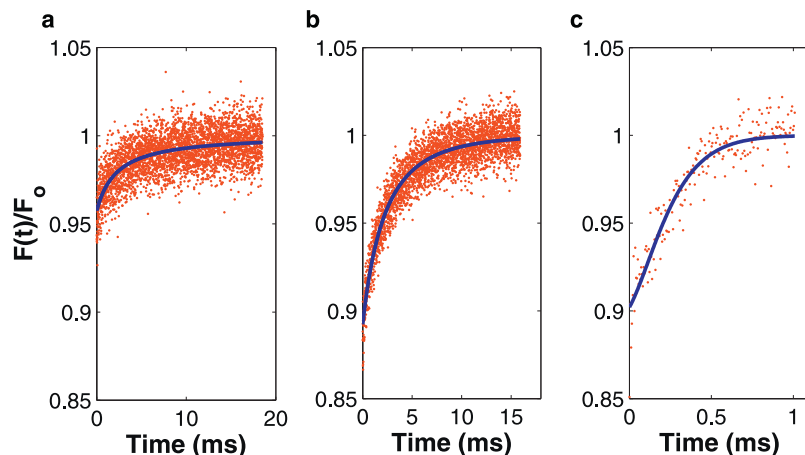


FIGURE 7 Experimental fluorescence recovery curves of FITC-dextran, flowing in vessels of 4T1 tumors growing in dorsal skinfold chambers. Each curve represents a different fitting regime for the diffusion-convection model. (a) Diffusion-dominated recovery; only the diffusion coefficient is accurately determined. (b) Balanced recovery; both the diffusion coefficient and flow speed are accurately determined. (c) Flow-dominated recovery; only the flow speed is accurately determined.

the diffusion-only MP-FRAP model and comfortably within the diffusion-dominated regime for the diffusion-convection model. From this, we would predict that both models would yield an accurate value for the diffusion coefficient, and that the diffusion-convection model would provide an inaccurate value for the flow speed. As predicted, the two models produce identical values for the diffusion coefficient ($D = 9.28 \mu\text{m}^2/\text{s}$), which is consistent with the literature when adjusted via the Stokes-Einstein relation using a plasma viscosity of $\eta = 1.2 \text{ cP}$. Meanwhile, as predicted, a significant difference is evident between the measured flow speed ($v = 0.02 \pm 2000 \mu\text{m}/\text{s}$) and the RBC speed ($v = 14 \pm 3 \mu\text{m}/\text{s}$).

Vessel 2 has a predicted scaled speed of 0.45 ± 0.05 , which is above the cutoff speed for the diffusion-only model but within the balanced regime for the diffusion-convection model. This indicates that the diffusion-only model should overestimate the diffusion coefficient, while the diffusion-convection model should yield accurate results for both the diffusion coefficient and the flow speed. As expected, the diffusion-only model produces an erroneously high diffusion coefficient ($D = 19.6 \pm 0.4 \mu\text{m}^2/\text{s}$) due to the presence of significant flow. In addition, as predicted, the diffusion-convection model produces a diffusion coefficient ($D = 9.68 \pm 0.34 \mu\text{m}^2/\text{s}$) that compares well with the value obtained from vessel 1 and with the extrapolated literature value. This suggests that this measurement is not impacted by the increased flow speed. Additionally, the diffusion-convection model yields a result for the flow speed that is comparable to the RBC speed. The slight difference between the plasma speed produced by the diffusion-convection

model and the RBC speed produced by the line-scans is statistically significant (69.3 ± 1.0 versus $80 \pm 10 \mu\text{m}/\text{s}$, $p = 0.036$). However, on the edge of the red blood cell-free layer within blood vessels, it is expected that the RBC speed will be slightly larger than the plasma speed (44).

Vessel 3 has a predicted scaled speed of 6.2, well above the cutoff speed for the diffusion-only model and in the flow-dominated regime for the diffusion-convection model. From this, we expect both models to yield inaccurate results for the diffusion coefficient, while the diffusion-convection model should provide an accurate measure of the flow speed. As predicted, the diffusion-only model produces a diffusion coefficient that is erroneously high ($D = 250 \pm 24 \mu\text{m}^2/\text{s}$), due to the presence of dominant flow. The diffusion-convection model also produces an erroneously high diffusion coefficient ($D = 34.9 \pm 9.5 \mu\text{m}^2/\text{s}$). This suggests that the flow in this vessel is rapid enough to produce detectable deviations in diffusion coefficient measurements, even for the diffusion-convection model. Finally, the plasma speed determined by the diffusion-convection model is comparable to the RBC speed, although the small difference between the measured flow speed and the RBC speed is statistically significant (987 ± 36 versus $1140 \pm 80 \mu\text{m}/\text{s}$, $p = 0.013$). This small difference is again anticipated in tumor vessels, and allows us to conclude that the fit speed value is accurate.

DISCUSSION

MP-FRAP is a well-established microscopy technique used to measure the diffusion of macromolecules within biological

TABLE 1 Results of fitting experimental in vivo data of diffusion and convection in tumor vessels using both the diffusion-only and diffusion-convection models

	v_s^*	$D_d^\dagger (\mu\text{m}^2/\text{s})$	$D_{d-c}^\dagger (\mu\text{m}^2/\text{s})$	$v_{d-c}^\dagger (\mu\text{m}/\text{s})$	$v_{\text{RBC}}^* (\mu\text{m}/\text{s})$
Vessel 1	0.08 ± 0.02	9.3 ± 0.5	9.3 ± 0.5	0.02 ± 2000	14 ± 3
Vessel 2	0.45 ± 0.05	19.6 ± 0.4	9.7 ± 0.3	70 ± 1	80 ± 10
Vessel 3	6.2 ± 0.4	250 ± 25	35 ± 10	990 ± 40	1140 ± 80

*Reported error is \pm error of the mean, $n = 5$.

† Reported error is \pm standard error in fitted parameter, $n = 1$.

systems. However, the presence of unanticipated convective flow can produce erroneous diffusion coefficients when recovery curves are fit with the previously derived diffusion-only model. Here we have derived a new diffusion-convection model for fitting MP-FRAP recovery curves, which improves upon the diffusion-only model by enabling accurate determination of the diffusion coefficient in the presence of significant convective flows. We have evaluated this new model by fitting computer-generated recovery curves with convective flow and by conducting *in vitro* experiments with known flows and known diffusion coefficients as a means of evaluating the physical accuracy of the model and quantifying the advantages of the diffusion-convection model compared with the diffusion-only model. We have also demonstrated the new MP-FRAP model in measurements of the diffusion coefficient and flow speed *in vivo* within tumor blood vessels.

Diffusion-only MP-FRAP model

As shown in Figs. 3 and 5, the diffusion-only model yields accurate values for the diffusion coefficient at negligible flows in both computer-generated data and *in vitro* experiments. As flows become appreciable and increase the rate of recovery, the diffusion-only model compensates by erroneously raising the diffusion coefficient in the resulting fit. At extremely high flow speeds, this error is obvious to the experimentalist as the shape of the recovery curve changes dramatically and the diffusion-only model fit becomes visibly poor (Fig. 8 *a*). However, when flow only moderately influences the recovery, the shape change is subtle and the diffusion-only model may still yield a good looking fit while offering an inaccurate diffusion coefficient (Fig. 8 *b*). Herein lies the danger when the diffusion-only model is applied to an unfamiliar system with modest convective flow. This effect can be quantified with our experimentally derived cutoff scaled speed of $v_s \approx 0.3$. For scaled speeds greater than this value, at typical relative noise values, fitting with

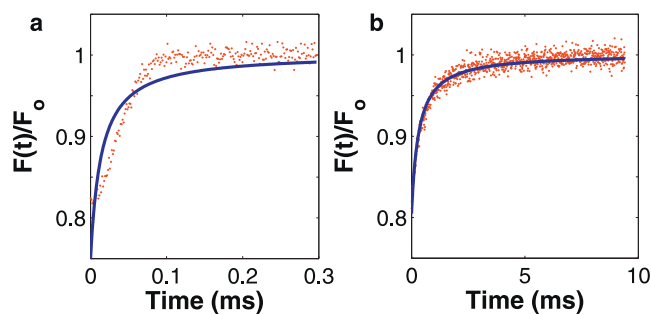


FIGURE 8 Computer-generated fluorescence recovery curves, generated with the diffusion-convection model and fit to the diffusion-only model. (a) The recovery is flow-dominated and there is an obvious alteration in the shape of the recovery curve, which is visibly poorly fit by the diffusion-only model. (b) The recovery is balanced under the influences of diffusion and flow. Although the fit looks good by eye, the diffusion-only model produces a diffusion coefficient 25% larger than the input value.

the diffusion-only model will yield erroneous values of the diffusion coefficient.

Diffusion-convection MP-FRAP model

The diffusion-convection model offers a significant improvement over the diffusion-only model by yielding accurate diffusion coefficients in the presence of flows significant enough to generate errors in the diffusion coefficient when fit by the diffusion-only model. As an added benefit, the diffusion-convection model is also capable of accurately determining the flow speed over some range of parameters. However, fits to computer-generated and *in vitro* data show that when either diffusion or flow dominates the fluorescence recovery, the diffusion-convection model poorly determines the nondominant parameter, thus setting up three regimes: 1), diffusion-dominated, in which only the diffusion coefficient is accurately determined; 2), balanced, in which both the diffusion coefficient and flow speed are accurately determined; and 3), flow-dominated, in which only the flow speed is accurately determined. By defining a scaled speed parameter, $v_s = v(\omega_r/8D)$, each of the two transitions between the regimes can be seen to occur over the same range of scaled speeds for all magnitudes of diffusion coefficients. These transitions will shift slightly when fluorescence recoveries with differing amounts of relative noise and/or bleach depths are analyzed, such that the balanced regime is broadest with low noise and/or high bleach depth and is narrowest with high noise and/or low bleach depth.

As a direct experimental measure of the abilities of the diffusion-convection model, we conducted MP-FRAP in a simple system with known flow speeds, using a fluorescent dye conjugated to a macromolecule (BSA or dextran) with a known diffusion coefficient. In agreement with the fits to computer-generated data, a comparison of fits of the *in vitro* data to the diffusion-only and diffusion-convection models showed that the diffusion-convection model yields accurate diffusion coefficients for flow speeds up to ~ 10 times the value of the maximum speed at which the diffusion-only model was able to yield an accurate diffusion coefficient. In addition, as expected, when flow speeds were appreciable yet small, the diffusion-convection model accurately determined the diffusion coefficient, but poorly determined the flow speed. Specifically, for typical experimental noise ($\sim 4\%$) and bleach depth (~ 0.5), the cutoff speed for transition from diffusion-dominated to balanced recoveries was $v_s \approx 0.2$, while the cutoff speed for transition from balanced to flow-dominated recoveries was $v_s \approx 3$. For both transitions, the standard deviation of the measured value of the nondominant parameter was a more sensitive indicator of problems with the fit than was the average value of the nondominant parameter. We also applied the diffusion-convection model to recovery curves taken in the presence of axial flows (perpendicular to the imaging plane), and showed that the model correctly recovers the diffusion coefficient. By

extension, with a priori knowledge of the flow direction, the diffusion-convection model could be used to determine the diffusion coefficient (and flow speed) for multidimensional flows without increasing the number of fitting parameters.

It is also important to note that the choice of tracer molecule significantly affects the ability to accurately measure the diffusion coefficient in the presence of convective flow. Given that the cutoff scaled speed values are constant with relation to the value of the diffusion coefficient, and that $v_s = v(\omega_r/8D)$, we see that the larger the diffusion coefficient is for a given tracer, the smaller the scaled speed will be for any particular absolute speed. To keep the scaled speed below the cutoff between the balanced and flow-dominated regimes (where diffusion can no longer be accurately measured), systems with large flow speeds are best probed with small molecules (typically having a large diffusion coefficient), whereas systems with small flow speeds are as accurately probed with small or large molecules (typically having a large or small value of the diffusion coefficient, respectively).

In vivo application

As an analogous demonstration of the diffusion-convection model in vivo to compare with our in vitro results, we chose to measure diffusion and convection within tumor blood vessels. The RBC speed provided a separate indicator of flow speeds with which to evaluate our model. Our first example was a vessel with an extremely slow RBC speed, and hence a low scaled speed of 0.08 (calculated using our in vitro values of the diffusion coefficient extrapolated to plasma at 37°C). From this scaled speed value, we predicted that accurate values for the diffusion coefficient would be produced by both the diffusion-only and the diffusion-convection models, but that an inaccurate value for the flow speed would be given by the diffusion-convection model, due to the dominance of diffusion over flow. Our second example was a vessel with a scaled speed of 0.45, in between the two transition cutoff speeds, suggesting that the diffusion-only model would be unable to produce an accurate value for the diffusion coefficient, while the diffusion-convection model would accurately determine both the diffusion coefficient and flow speed. Our third example was a vessel with a scaled speed of 6.24, above the highest transition cutoff speed, and predicting inaccurate values for the diffusion coefficient from both models, but an accurate flow speed from the diffusion-convection model. In each case, the in vivo data analyzed as predicted. These examples demonstrate in vivo that the diffusion-convection model extends the range of flow speeds over which accurate diffusion coefficients can be determined by an order of magnitude and that the diffusion-convection model can also determine the flow speed accurately over a wide range of flows.

In addition to the diffusion-convection model described here, an anomalous subdiffusion model has been derived and used as an alternative to the diffusion-only model to fit

FRAP and in vivo MP-FRAP curves (37,45,46). An anomalous subdiffusion model can be produced by replacing any Dt terms in the recovery equation (Eq. 3) with Γt^α , where Γ is a constant transport coefficient with units $\mu\text{m}^2/\text{s}^\alpha$ and $0 < \alpha < 1$ (37). Choosing between models is straightforward, as anomalous subdiffusion and convective flow differentially affect the speed of recovery and the shape of the recovery curve. Graphically, anomalous subdiffusion stretches out MP-FRAP curves, while convective flow adds a kink. By again using computer-generated MP-FRAP curves, we determined that the two models are incompatible. Recovery curves generated using the diffusion-convection model could be fit by the anomalous subdiffusion model with a low χ -squared value, but in the presence of significant convective flow, the added kink causes the anomalous subdiffusion model to produce parameter values grossly out of line with the literature. For example, for a curve generated with $v_s = 1$ (within the balanced regime), the resulting fit to the anomalous subdiffusion model yielded $\Gamma = 1.35 \times 10^6 \mu\text{m}^2/\text{s}^\alpha$ and $\alpha = 2.11$ (Fig. 9 a), compared with $\Gamma = 0.7 \mu\text{m}^2/\text{s}^\alpha$ and $\alpha = 0.55$ found in the literature (37). Meanwhile, in the presence of significant anomalous subdiffusion, the stretching-out of the curve is visibly very poorly fit by the diffusion-convection model (Fig. 9 b). Of course, in ranges with mildly anomalous subdiffusion ($\alpha > 0.85$, i.e., close to 1) or small scaled flow speeds ($v_s < 0.1$, i.e., close to 0), low χ -squared fits with reasonable parameter values are produced. In these cases, some a priori knowledge of the system would be necessary to distinguish mildly anomalous subdiffusion from a slow transverse flow speed.

Future applications

In future experiments in which both the diffusion coefficient and flow speed are not known a priori, the diffusion-convection model can be used for fitting MP-FRAP curves, and the typical cutoff speeds determined here can act as a retrospective

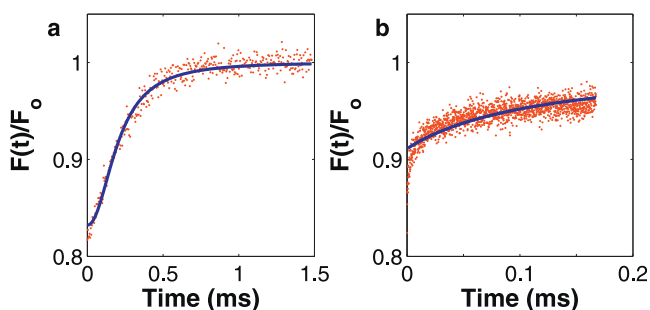


FIGURE 9 Mismatch between diffusion-convection and anomalous subdiffusion models. (a) Curve was computer-generated with the diffusion-convection model ($D = 52 \mu\text{m}^2/\text{s}$ and $v_s = 1$) and fit with the anomalous subdiffusion model. Although the fit looks good, the anomalous parameters are grossly misaligned with the literature ($\Gamma = 1.35 \times 10^6 \mu\text{m}^2/\text{s}^\alpha$ and $\alpha = 2.11$). (b) Curve was computer-generated with the anomalous subdiffusion model ($\Gamma = 0.7 \mu\text{m}^2/\text{s}^\alpha$ and $\alpha = 0.35$) and fit with the diffusion-convection model. The fit is visibly poor ($D = 172.08 \mu\text{m}^2/\text{s}$ and $v = 0.13 \mu\text{m}/\text{s}$).

sanity check. If the output diffusion coefficient and flow speed are within the cutoff speeds, one can assume the values are correct. This is because at no point does the absolute error in the nondominant parameter grow large enough to map the incorrect output parameters into the balanced regime. For example, the computer-generated MP-FRAP curves that produced the data on the extreme right-hand side of Fig. 4 were performed at a scaled speed of 300 and produced a normalized diffusion coefficient of 10 and a normalized flow speed of 1. The output scaled speed is hence (incorrectly) determined to be 30. This scaled speed value is erroneously low, but still above the cutoff speed, and hence would be easily rejected by the experimentalist as indicating incorrect values of the fit parameters, even if the fit appears reasonable.

CONCLUSION

In this article, we derived an improved model of multiphoton fluorescence recovery after photobleaching that explicitly accounts for the presence of convective flow, as well as diffusion. Using computer-generated data to guide our in vitro experiments, we demonstrated that this new model extends the ability of MP-FRAP to determine diffusion coefficients accurately in the presence of flow to flow speeds an order-of-magnitude higher than is possible with the diffusion-only model of MP-FRAP, which does not account for flow. We also determined experimentally useful cutoff speeds that, for typical experimental parameters, predict the range of scaled speeds over which the diffusion-convection model allows MP-FRAP to produce accurate diffusion coefficients, as well as accurate flow speeds.

APPENDIX

The time-dependent concentration of unbleached fluorophore immediately after the termination of a bleach pulse is given by Brown et al. (37). When converted to Cartesian coordinates, this is given by

$$c(x, y, z; t) = \sum_{n=0}^{\infty} A_n(t) e^{-\mu_n(t)x^2} e^{-\mu_n(t)y^2} e^{-\nu_n(t)z^2}, \quad (4)$$

where

$$A_n(t) = c_0 \frac{(-\beta)^n}{n!} \frac{1}{(1 + 8bnDt/\omega_r^2)(1 + 8bnDt/\omega_z^2)^{1/2}}, \quad (5)$$

$$\mu_n(t) = \frac{2bn}{\omega_r^2} \frac{1}{(1 + 8bnDt/\omega_r^2)}, \quad (6)$$

$$\nu_n(t) = \frac{2bn}{\omega_z^2} \frac{1}{(1 + 8bnDt/\omega_z^2)}. \quad (7)$$

An attenuated laser beam is used to monitor the changing concentration profile. The fluorescence recovery is given by (37)

$$F(t) = \frac{\delta_m E}{m} \int \langle I_{mo}^m(x, y, z) \rangle c(x, y, z; t) dx dy dz, \quad (8)$$

where δ_m is the multiphoton fluorescence action cross section, $\langle I_{mo}^m(x, y, z) \rangle$ is the time-average of the bleach intensity raised to the m^{th} power, and m is the number of photons required to produce fluorescence from a single fluorophore.

We first consider flow along the x axis. To solve for $F(t)$ in this case, we choose a frame of reference in which we have a source moving along the x direction (the concentration distribution moving under flow) and a stationary observer (the focal volume monitoring the intensity). In the frame of reference of the observer, $x' = x + vt$, $y' = y$, and $z' = z$. The time-dependent fluorophore concentration is now

$$c(x', y', z'; t) = \sum_{n=0}^{\infty} A_n(t) e^{-\mu_n(t)(x'-vt)^2} e^{-\mu_n(t)y'^2} e^{-\nu_n(t)z'^2}. \quad (9)$$

The expression for the monitoring intensity distribution does not change from the case of both source and observer stationary (37):

$$\langle I_{mo}^m(x', y', z') \rangle = \langle I_o \rangle e^{-(2m/\omega_r^2)x'^2} e^{-(2m/\omega_r^2)y'^2} e^{-(2m/\omega_z^2)z'^2}. \quad (10)$$

Substituting Eqs. 9 and 10 into Eq. 8 yields

$$F(t) = \frac{\delta_m E}{m} \langle I_o \rangle \sum_{n=0}^{\infty} A_n(t) \int_{-\infty}^{+\infty} e^{-\mu_n(t)(x'-vt)^2 - (2m/\omega_r^2)x'^2} dx' \\ \times \int_{-\infty}^{+\infty} e^{-(\mu_n(t) + 2m/\omega_r^2)y'^2} dy' \int_{-\infty}^{+\infty} e^{-(\nu_n(t) + 2m/\omega_z^2)z'^2} dz'. \quad (11)$$

Before integrating, we first rewrite the exponential in x' by expanding the exponent, completing the square in x' , then making the variable substitution:

$$\gamma' = x' - \frac{\mu_n(t)vt}{\mu_n(t) + 2m/\omega_r^2}. \quad (12)$$

The expression for the fluorescence recovery now looks like

$$F(t) = \frac{\delta_m E}{m} \langle I_o \rangle \sum_{n=0}^{\infty} \bar{A}_n(t) \int_{-\infty}^{+\infty} e^{-(\mu_n(t) + 2m/\omega_r^2)\gamma'^2} d\gamma' \\ \times \int_{-\infty}^{+\infty} e^{-(\mu_n(t) + 2m/\omega_r^2)y'^2} dy' \int_{-\infty}^{+\infty} e^{-(\nu_n(t) + 2m/\omega_z^2)z'^2} dz', \quad (13)$$

where

$$\bar{A}_n(t) = A_n(t) \exp \left[-\frac{2m\mu_n(t)v^2 t^2}{2m + \mu_n(t)\omega_r^2} \right]. \quad (14)$$

The integrals in Eq. 13 are now all first-order Gaussians. When the integrals are performed and $\bar{A}_n(t)$, $\mu_n(t)$, and $\nu_n(t)$ have been substituted in, the simplified expression, letting $m = b = 2$ for a two-photon process, is

$$F(t) = F_o \sum_{n=0}^{\infty} \frac{(-\beta)^n}{n!} \\ \times \frac{\exp \left[-\frac{4n(vt/\omega_r)^2}{1 + n + 16nDt/\omega_r^2} \right]}{(1 + n + 16nDt/\omega_r^2)(1 + n + 16nDt/\omega_z^2)^{1/2}}. \quad (15)$$

We may also express the equation in terms of system-specific variables, $\tau_D = \omega_r^2/8D$ and $\tau_v = \omega_r/v$:

$$F(t) = F_0 \sum_{n=0}^{\infty} \frac{(-\beta)^n}{n!} \exp \left[-\frac{4n(t/\tau_v)^2}{1+n+2nt/\tau_D} \right] \times \frac{1}{(1+n+2nt/\tau_D)(1+n+2nt/R\tau_D)^{1/2}}. \quad (16)$$

This equation can be generalized to flow with a component along all three axes ($v^2 = v_x^2 + v_y^2 + v_z^2$) as

$$F(t) = F_0 \sum_{n=0}^{\infty} \frac{(-\beta)^n}{n!} \exp \left[-\frac{4nt^2(1/\tau_{v_x}^2 + 1/\tau_{v_y}^2)}{1+n+2nt/\tau_D} \right] \exp \left[-\frac{4nt^2/\tau_{v_z}^2}{1+n+2nt/R\tau_D} \right] \times \frac{1}{(1+n+2nt/\tau_D)(1+n+2nt/R\tau_D)^{1/2}}, \quad (17)$$

where $\tau_{v_x} = \omega_r/v_x$, $\tau_{v_y} = \omega_r/v_y$, and $\tau_{v_z} = \omega_r/v_z$. Finally, we can express this equation in cylindrical coordinates, to mimic the symmetry of the two-photon focal volume,

$$F(t) = F_0 \sum_{n=0}^{\infty} \frac{(-\beta)^n}{n!} \exp \left[-\frac{4nt^2/\tau_{v_r}^2}{1+n+2nt/\tau_D} \right] \exp \left[-\frac{4nt^2/\tau_{v_z}^2}{1+n+2nt/R\tau_D} \right] \times \frac{1}{(1+n+2nt/\tau_D)(1+n+2nt/R\tau_D)^{1/2}}, \quad (18)$$

where $\tau_{v_r} = \omega_r/v_r$ and $\tau_{v_z} = \omega_r/v_z$. Note that v_r is not a radial velocity (this would imply a divergence), but rather the resultant velocity obtained by adding the velocity components within the image plane (v_x and v_y) vectorially. Because the radial and axial dimensions of the two-photon focal volume are not equal, the velocity components parallel and perpendicular to the image plane cannot be combined into a coordinate-free resultant velocity. The decision to use Eq. 16, 17, or 18 depends on the experimentalist's knowledge of the direction of the flow. Use of the one-dimensional form, Eq. 16, is justified in this work because the in vitro experiments were designed to allow flow predominantly in one direction and the flow within blood vessels, measured in vivo, is directed parallel to the vessel wall.

Special thanks to Ryan Burke for overseeing all cell and tissue culture, and to Khawarl Liverpool for his careful dorsal skinfold chamber surgeries.

This work was funded by a Department of Defense Era of Hope Scholar Award (No. W81XWH-05-1-0396) and a Pew Scholar in the Biomedical Sciences Award to E.B.B. III.

REFERENCES

- Peters, R., J. Peters, K. Tews, and W. Bahr. 1974. Microfluorimetric study of translational diffusion of proteins in erythrocyte membranes. *Biochim. Biophys. Acta*. 367:282–294.
- Axelrod, D., D. E. Koppel, J. Schlessinger, E. Elson, and W. W. Webb. 1976. Mobility measurement by analysis of fluorescence photobleaching recovery kinetics. *Biophys. J.* 16:1055–1069.
- Edidin, M., M. Zagyansky, and T. Lardner. 1976. Measurement of membrane protein lateral diffusion in single cells. *Science*. 191:466–468.
- Schlessinger, J., D. E. Koppel, D. Axelrod, K. Jacobson, W. W. Webb, et al. 1976. Lateral transport on cell membranes: mobility of concanin A receptors on myoblasts. *Proc. Natl. Acad. Sci. USA*. 73:2409–2413.
- Tsay, T.-T., and K. A. Jacobson. 1991. Spatial Fourier analysis of video photobleaching measurements. *Biophys. J.* 60:360–368.
- Berk, D. A., F. Yuan, M. Leunig, and R. K. Jain. 1993. Fluorescence photobleaching with spatial Fourier analysis: measurement of diffusion in light-scattering media. *Biophys. J.* 65:2428–2436.
- Denk, W., J. H. Strickler, and W. W. Webb. 1990. Two-photon laser scanning fluorescence microscopy. *Science*. 248:73–76.
- Brown, E. B., R. B. Campbell, Y. Tsuzuki, L. Xu, P. Carmeliet, et al. 2001. In vivo measurement of gene expression, angiogenesis, and physiological function in tumors using multi-photon laser scanning microscopy. *Nat. Med.* 7:864–868.
- Brown, E. B., Y. Boucher, S. Nasser, and R. K. Jain. 2004. Measurement of macromolecular diffusion coefficients in human tumors. *Microwasc. Res.* 67:231–236.
- Dunn, K. W., R. M. Sandoval, K. J. Kelly, P. C. Dagher, G. A. Tanner, et al. 2002. Functional studies of the kidney of living animals using multicolor two-photon microscopy. *Am. J. Physiol. Cell Physiol.* 283:C905–C916.
- Molitoris, B. A., and R. M. Sandoval. 2005. Intravital multiphoton microscopy of dynamic renal processes. *Am. J. Physiol. Renal Physiol.* 288:F1084–F1089.
- Sipos, A., I. Toma, J. Kang, L. Rosivall, and J. Peti-Peterdi. 2007. Advances in renal (patho)physiology using multiphoton microscopy. *Kidney Int.* 72:1188–1191.
- Rosivall, L., S. Mirzahassemi, I. Toma, A. Sipos, and J. Peti-Peterdi. 2006. Fluid flow in the juxtaglomerular interstitium visualized in vivo. *Am. J. Physiol. Renal Physiol.* 291:1241–1247.
- Kuricheti, K. K., V. Buschmann, and K. D. Weston. 2004. Application of fluorescence correlation spectroscopy for velocity imaging in microfluidic devices. *Appl. Spectrosc.* 58:1180–1186.
- Squires, T., and S. Quake. 2005. Microfluidics: fluid physics at the nanoliter scale. *Rev. Mod. Phys.* 77:977–1026.
- Kim, D. R., and X. Zheng. 2008. Numerical characterization and optimization of the microfluidics for nanowire biosensors. *Nano Lett.* 8:3233–3237.
- Késmárky, G., P. Kenyeres, M. Rábai, and K. Tóth. 2008. Plasma viscosity: a forgotten variable. *Clin. Hemorheol. Microcirc.* 39:243–246.
- James, D. R. 1974. The hyperviscosity syndrome. *Br. J. Oral Surg.* 12:56–62.
- Junker, R., J. Heinrich, H. Ulbrich, H. Schulte, R. Schönfeld, et al. 1998. Relationship between plasma viscosity and the severity of coronary heart disease. *Arterioscler. Thromb. Vasc. Biol.* 18:870–875.
- Kensley, K. R. 2003. The mechanistic relationships between hemorheological characteristics and cardiovascular disease. *Curr. Med. Res. Opin.* 19:587–596.
- Lowe, G., F. Fowkes, J. Dawes, P. Donnan, S. Lennie, et al. 1993. Blood viscosity, fibrinogen, and activation of coagulation and leukocytes in peripheral arterial disease and the normal population in the Edinburgh Artery Study. *Circulation*. 87:1915–1920.
- Coull, B. M., N. Beamer, P. de Garmo, G. Sexton, F. Nordt, et al. 1991. Chronic blood hyperviscosity in subjects with acute stroke, transient ischemic attack, and risk factors for stroke. *Stroke*. 22:162–168.
- Mehta, J., and S. Singhal. 2003. Hyperviscosity syndrome in plasma cell dyscrasias. *Semin. Thromb. Hemost.* 29:467–471.
- von Tempelhoff, G.-F., L. Heilmann, G. Hommel, and K. Pollow. 2003. Impact of rheological variables in cancer. *Semin. Thromb. Hemost.* 29:499–513.

25. International Committee for Standardization in Hematology. 1998. Guidelines on selection of laboratory tests for monitoring the acute phase response. *J. Clin. Path.* 41:1203–1212.
26. Berk, D. A., M. A. Swartz, A. J. Leu, and R. K. Jain. 1996. Transport in lymphatic capillaries. II. Microscopic velocity measurement with fluorescence photobleaching. *Am. J. Physiol.* 270:H330–H337.
27. Chary, S. R., and R. K. Jain. 1989. Direct measurement of interstitial convection and diffusion of albumin in normal and neoplastic tissues by fluorescence photobleaching. *Proc. Natl. Acad. Sci. USA.* 86:5385–5389.
28. Jain, R. K., R. J. Stock, S. R. Chary, and M. Rueter. 1990. Convection and diffusion measurements using fluorescence recovery after photobleaching and video calibration. *Microvasc. Res.* 39:77–93.
29. Mudge, D., W. W. Webb, and E. L. Elson. 1974. Fluorescence correlation spectroscopy. III. Uniform translation and laminar flow. *Biopolymers.* 17:361–376.
30. Qian, H., M. P. Sheetz, and E. L. Elson. 1991. Single particle tracking. Analysis of diffusion and flow in two-dimensional systems. *Biophys. J.* 60:910–921.
31. Saxton, M. J., and K. Jacobson. 1997. Single-particle tracking: applications to membrane dynamics. *Annu. Rev. Biophys. Biomed.* 26:373–399.
32. Berland, K. M., P. T. C. So, and E. Gratton. 1995. Two-photon fluorescence correlation spectroscopy: method and application to the intracellular environment. *Biophys. J.* 68:694–701.
33. Mertz, J., C. Xu, and W. W. Webb. 1995. Single-molecule detection by two-photon excited fluorescence. *Opt. Lett.* 20:2532–2534.
34. Wiseman, P. W., J. A. Squier, M. H. Ellisman, and K. R. Wilson. 2000. Two photon image correlation spectroscopy and image cross-correlation spectroscopy. *J. Microsc.* 200:14–25.
35. Kolin, D. L., D. Ronis, and P. W. Wiseman. 2006. k-space image correlation spectroscopy: a method for accurate transport measurements independent of fluorophore photophysics. *Biophys. J.* 91:3061–3075.
36. Hebert, B., S. Costantino, and P. W. Wiseman. 2005. Spatiotemporal image correlation spectroscopy (STICS) theory, verification, and application to protein velocity mapping in living CHO cells. *Biophys. J.* 88:3601–3614.
37. Brown, E. B., E. S. Wu, W. Zipfel, and W. W. Webb. 1999. Measurement of molecular diffusion in solution by multiphoton fluorescence photobleaching recovery. *Biophys. J.* 77:2837–2849.
38. Kleinfeld, D., P. P. Mitra, F. Helmchen, and W. Denk. 1998. Fluctuations and stimulus-induced changes in blood flow observed in individual capillaries in layers 2 through 6 of rat neocortex. *Proc. Natl. Acad. Sci. USA.* 95:15741–15746.
39. Leunig, M., F. Yuan, M. D. Menger, Y. Boucher, A. E. Goetz, et al. 1992. Angiogenesis, microvascular architecture, microhemodynamics, and interstitial fluid pressure density during early growth in human adenocarcinoma LS 174T in SCID mice. *Cancer Res.* 52:6553–6560.
40. Lanni, F., D. L. Taylor, and B. R. Ware. 1981. Fluorescence photobleaching recovery in solutions of labeled actin. *Biophys. J.* 35:351–364.
41. Bor Fuh, C., S. Levin, and J. C. Giddings. 1993. Rapid diffusion coefficient measurements using analytical SPLITT fractionation: application to proteins. *Anal. Biochem.* 208:80–87.
42. Pluen, A., P. A. Netti, R. K. Jain, and D. A. Berk. 1999. Diffusion of macromolecules in agarose gels: comparison of linear and globular configurations. *Biophys. J.* 77:542–552.
43. Pluen, A., Y. Boucher, S. Ramanujan, T. D. McKee, T. Gohongi, et al. 2001. Role of tumor-host interactions in interstitial diffusion of macromolecules: cranial vs. subcutaneous tumors. *Proc. Natl. Acad. Sci. USA.* 98:4628–4633.
44. Jain, R. K. 1988. Determinants of tumor blood flow: a review. *Cancer Res.* 48:2641–2658.
45. Feder, T. J., I. Brust-Mascher, J. P. Slattery, B. Baird, and W. W. Webb. 1996. Constrained diffusion or immobile fraction on cell surfaces: a new interpretation. *Biophys. J.* 70:2767–2773.
46. Perisamy, N., and A. S. Verkman. 1998. Analysis of fluorophore diffusion by continuous distributions of diffusion coefficients: applications of photobleaching measurements of multicomponent and anomalous diffusion. *Biophys. J.* 75:557–567.

Thermally Activated Diffusion in Reversibly Associating Polymers

Jiahui Li,^a Kelley Sullivan,^b Edward Brown,^c and Mitchell Anthamatten^{*,a}

Received (in XXX, XXX) Xth XXXXXXXXX 200X, Accepted Xth XXXXXXXXX 200X

First published on the web Xth XXXXXXXXX 200X

DOI: 10.1039/b000000x

Mass transport of a small molecule dye through dynamic polymer networks containing reversibly associating side-groups was directly compared to steady-shear viscosity measurements and indicates that viscous relaxation is limited by the frequency of dissociation events while mass transport is determined by the degree of association.

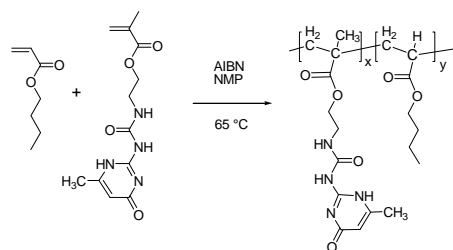
The mission to understand structure-property relationships of polymers bearing reversibly associating functional groups has opened a new field at the interface of polymers and supramolecular chemistry. Reversible binding through cooperative hydrogen bonds, ionic interactions, and metal-ligand complexes can lead to aggregation, gelation, or sudden viscosity changes that are triggered by changes in polymer concentration, pH, or temperature.^{1, 2} In the melt, rigid and elastic dynamic networks can be transformed into low viscosity melts, simply by heating. This material concept has engendered new shape memory polymers, thermoplastic elastomers, and self-healing materials.³⁻⁵ These and other studies have highlighted the role that reversible interactions play in influencing the dynamics of viscous relaxation.

Understanding the dissociation kinetics of supramolecular polymers is paramount in developing responsive materials. Dissociation of dimers or aggregates is thermally activated and can be directly related to mechanical properties.^{3, 6-8} At low temperatures, the rate of dissociation is sluggish and limits viscous relaxation of chains. At higher temperatures reversible interactions exhibit rapid exchange resulting in lower modulus and rapid stress relaxation.

To our knowledge, no singular study has been performed to examine how mass transport of small molecules through polymer melts is influenced by reversible interactions. Understanding and controlling mass transport through amorphous polymers is an important aspect of emerging technologies including drug delivery, chemical sensors, and barrier elastomers. We are studying copolymer detailed relationships that connect H-bonding dynamics with rheological and mechanical properties containing reversibly associating side-groups. In this communication, we report a side-by-side comparison of how side-group association affects mechanical properties and mass transport in polymer melts. Our findings indicate that mass transport is not limited by the kinetics of side-group dissociation, but rather by the overall

equilibrium constant between free and associated side-groups.

A remarkably versatile H-bonding motif is the ureidopyrimidinone (UPy) functional group.² The UPy group contains four in-plane hydrogen bonds that act cooperatively to yield unusually high solution self-dimerization constants ($\sim 10^7 \text{ mol}^{-1}$ in CHCl_3).⁹ In addition to its high binding energy ($\sim 70 \text{ kJ/mol}$), the UPy group is an attractive synthon because it is straightforward synthesis. Reversibly Associating Copolymers (RACs) containing butyl acrylate and UPy-functionalized ethyl methacrylate monomers were prepared using conventional free radical polymerization (see Scheme 1). Polymerizations were conducted at 65°C for eight hours in N-methylpyrrolidone (NMP) using azobisisobutyronitrile (AIBN) as an initiator.⁴ The products were precipitated twice into a water/ methanol (1:10) solution to ensure the product was free of unreacted monomer. Functional polymers were characterized using ^1H NMR and gel permeation chromatography (Viscotek, Agilent 1100), and results are summarized in Table 1. The composition of polymer samples withdrawn after one-half-hour of reaction time (from ^1H NMR) showed close agreement with final product composition indicating that product polymers are nearly random copolymers and do not have significant composition gradients. Polymers were synthesized to nearly the same molecular weight ($\sim 15 \text{ kg/mol}$)— well below the entanglement molecular weight. Dye diffusion studies and steady-shear experiments were performed on purified copolymers and will be discussed in turn.



Scheme 1 Synthesis of poly (butyl acrylate) copolymer with UPy side-groups.

Table 1 Molecular weight characteristics of synthesized reversibly associating copolymers (RACs).

Name	UPy Content		M_n^b	PDI ^b
	Feed (mol %)	Measured ^a (mol %)		
PBA	0	0	14,100	1.53
RAC-1	1.0	0.84	16,500	2.00
RAC-2	2.0	1.68	12,600	2.11

a) ^1H NMR for aromatic vinyl hydrogen shift. b) GPC measurement performed at 60°C , with THF as eluent.

^a Department of Chemical Engineering, University of Rochester.

Rochester, NY 14627. E-mail: anthamatten@che.rochester.edu

^b Department of Physics and Astronomy, University of Rochester. Rochester, NY 14627

^c Department of Biomedical Engineering, University of Rochester. Rochester, NY 14627

Diffusion through synthesized polymers was studied using Multiphoton Fluorescence Recovery After Photobleaching (MP-FRAP, see Fig. 1). MP-FRAP measures 3-D mobility of fluorescent molecules with well defined bleaching geometry and a spatial resolution of less than a micron. FRAP is often used to study diffusion in biological systems, but has recently proven useful to study diffusion through polymer melts.¹⁰⁻¹² Unlike conventional (one photon) FRAP, the three-dimensional resolution of MP-FRAP renders it insensitive to sample thickness, facilitating measurement of bulk diffusion coefficient of dyes through the copolymers.

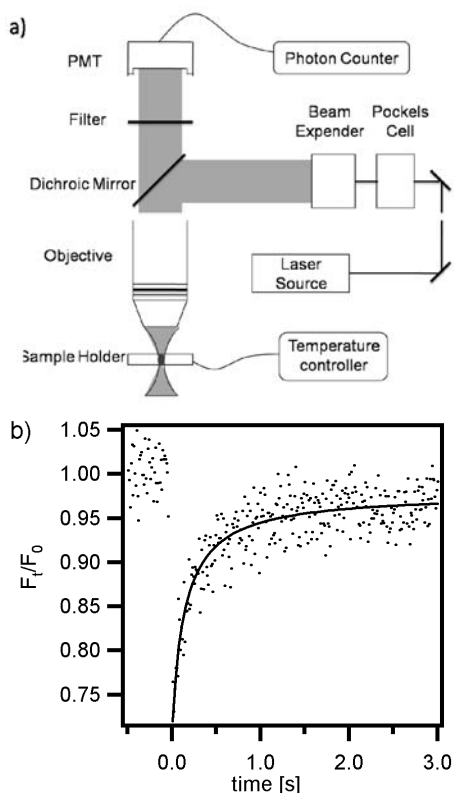


Fig. 1 MP-FRAP of reversibly associating polymers: a) experimental setup, and b) example of fluorescence recovery curve (RAC-1) with 20 M rhodamine 6G at 60 °C. This sample was photo-bleached using 810 nm light (350 mW) for 10 ms, and subsequent fluorescence was monitored at a reduced power of 35 mW. The dark line is a non-linear regression, least squares fit, to Equation 1 by varying β , F_0 and τ_D .

Diffusion of rhodamine 6G dye through synthesized polymers was studied between 20 and 80 °C. The fraction of recovered fluorescence, F_t/F_0 , was recorded against time t and fit using

$$F_t/F_0 = \sum_{n=0}^{\infty} \frac{2^{3/2}(-\beta)^n}{n!} \frac{1}{2 + 2n + 4nt/\tau_D} \frac{1}{\sqrt{2 + 2n + 4nt/R\tau_D}} \quad (1)$$

where β is the bleach depth; R and τ_D are defined by

$$R \equiv w_z^2/w_r^2 \quad (2)$$

and

$$\tau_D \equiv w_r^2/8D \quad (3)$$

where w_r and w_z are focal area radial and axial dimensions and D is the dye diffusion coefficient.¹³ Raw recovery data were fit using three parameters: β , F_0 and τ_D . The diffusion coefficient D was then obtained using Equation 3. Attempts were made fit only two parameters (β and τ_D), however the quality of fit was significantly lower. The two-parameter fitted curve typically overshoots the data at early time and results in a higher values of D . Nevertheless, both methods revealed similar trends leading to the same conclusion. To reduce uncertainty D , only values from three-parameter fits are reported.

An Arrhenius plot of measured dye diffusion coefficients through synthesized copolymers is shown in Fig. 2a. Clearly, the presence of associating side-groups inhibits dye diffusion. The greater the concentration of UPy-side groups, the lower the diffusion coefficient. However, the concentration of UPy side-groups has little effect on the diffusion activation energy, E_a , and all copolymers have about the same activation energies (~ 50 kJ/mol). This trend suggests that associating side-groups are behaving like permanent crosslinks over the temperature range studied.¹⁴ As a comparison, we prepared a crosslinked poly(butyl acrylate) containing 1 mol% ethylene glycol diacrylate (EGDA). The sample was loaded with dye and studied using MP-FRAP over the same temperature range. Resulting diffusion coefficients are shown in Fig. 2b. Comparing to Fig. 2a, it appears that non-covalent crosslinks hinder dye diffusion in same manner as permanent crosslinks. Both types of crosslinks lower the diffusion coefficient and do not significantly change the activation energy.

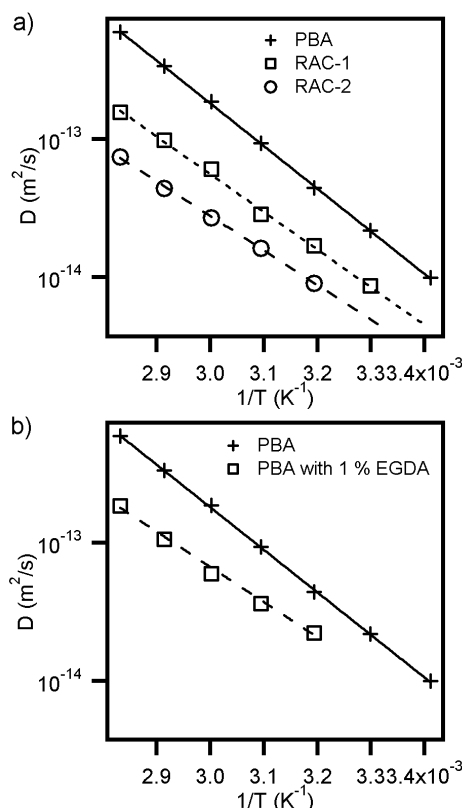


Fig. 2 Arrhenius plot of dye diffusion coefficient through reversibly associating polymers: a) poly(butyl acrylate) ($E_a = 59$ kJ/mol) and associating copolymers containing 0.8 and 1.7 mol% UPy side-groups ($E_a = 52$ kJ/mol, 48 kJ/mol) and b) poly(butyl acrylate) and crosslinked poly(butyl acrylate) with 1 mol % of EGDA as crosslinker ($E_a = 49$ kJ/mol).

Vrentas explained how solvent diffusion through polymer melts depends on temperature and crosslink density using a free volume theory.^{14, 15} Crosslinks inhibit diffusion by reducing polymer hole free volume \hat{V}_{FH} that is available for diffusive transport. This effect can be accounted for with a single temperature-independent parameter δ defined as:

$$\delta = \frac{\hat{V}_{FH,x}}{\hat{V}_{FH,0}} = \frac{\hat{V}_x^0}{\hat{V}_0^0} \quad (4)$$

where \hat{V}_x^0 and \hat{V}_0^0 are the specific volumes of the crosslinked and non-crosslinked polymers, and x defines the degree of crosslinking. Equation 4 is valid only if specific volumes (occupied, free, and interstitial) expand equally with temperature, and thermal expansion is independent of crosslink density. The Vrentas theory predicts that, in the limit of a dilute solvent diffusing through a lightly crosslinked polymer, the diffusion coefficient D_x scales with δ as

$$\ln \frac{D_x}{D_0} \propto \frac{(1-\delta)}{\delta} \quad (5)$$

To test equation 5, density measurements were performed to determine δ . The mass of single annealed polymer droplets situated on a glass cover-slips were measured using an electro-balance (Cahn 2000, $\pm 1 \mu\text{m}$). Profile images of the same droplets, from several different angles, were analytically fit (VCA Optima) and averaged to determine droplet volumes.

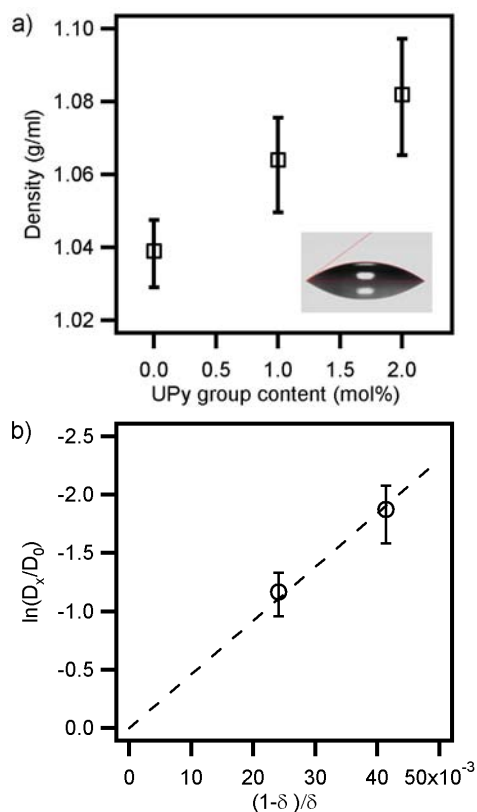


Fig. 3 a) Room temperature densities of synthesized polymers. Error bars are estimated from the uncertainty of the mass measurement ($\pm 1 \mu\text{g}$) and the standard deviation of the profile volume measurements (see text and inset). b) Plot illustrating that reduction in measured diffusivity is consistent with Eqn. 5. The quantity $\ln(D_x/D_0)$ was averaged at several different temperatures.

Results are displayed in Fig. 3. The density of linear poly(butyl acrylate) was measured to be 1.039 g/cm^3 and is within experimental error of the literature value.¹⁶ The densities of copolymers containing UPy groups were slightly higher, indicating lower specific volumes. Fig. 3 shows that diffusion is reduced according to $(1-\delta)/\delta$ (based on room temperature densities) as predicted by Equation 5. The agreement indicates that reversible crosslinks reduce the hole free volume available for transport in the same way that covalent crosslinks do.

Vrentas' theory also predicts a less pronounced, monotonic increase in the activation energy E_a with increasing x . While the data in Fig. 2 do not show E_a increases with associating side-group content, data do indicate that reversible crosslinking has little influence on E_a . Values of E_a are constant within experimental error for PBA, RAC-1, and RAC-2.

Where MP-FRAP uniquely enables molecular diffusion to be studied, it is well known that the rate of viscous relaxation of reversibly associating copolymers is thermally activated. At low temperatures, polymers containing associating groups exhibit higher storage modulus and melt viscosities compared to polymers without associating groups.²⁻⁴ Steady-shear experiments were conducted on synthesized polymers to enable a direct comparison of diffusion and stress relaxation dynamics. Viscosity data obtained at different temperatures are plotted in Fig. 4. Samples with higher UPy content showed higher viscosities and higher activation energies. This feature is consistent with our prior study of shape memory polymers which showed viscous relaxation is limited by the rate of side-group dissociation.³ Activation energies of linear PBA are in rough agreement with steady-shear data obtained by Yanamaguchi.⁴ Remarkably, the heightened activation

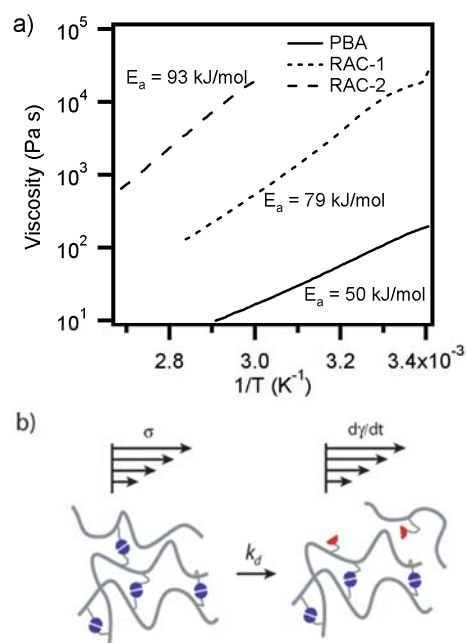


Fig. 4 a) Viscosities of polymers containing UPy H-bonding groups measured at a radial shear rate of 0.1 rad/s . b) Schematic illustrating viscous relaxation under shear stress (σ) in a dynamic polymer network containing self-complementary, reversible H-bonding groups.

energy observed in steady-shear experiments is clearly not observed in the MP-FRAP data (Fig. 2), suggesting a fundamental difference between diffusive transport through RACs and their viscous relaxation.

Together, steady-shear and MP-FRAP experiments suggest that, for the dynamic copolymers studied here, viscous relaxation is influenced by the H-bonding dissociation rate (k_d), while small molecule diffusion is determined by the H-bonding equilibrium value (K). In the case of steady-shear, when an H-bond dissociates, the material can more readily deform, under a lower stress field as indicated schematically in Fig. 4b. Consequently, shear rate and viscosity are inherently tied to the rate of H-bonding dissociation. This explains the observation of higher viscosities and higher activation energies for UPy containing polymers. A newly free associating group must find a similarly free species to bind with, and we predict that the extent of dimerization under shear may be also different than in a static state. This has not yet been confirmed experimentally.

On the other hand, small molecule diffusion through UPy containing copolymers is not under the influence of stress, associating groups can repeatedly dissociate and rebond with the same species. In this scenario, the relevant kinetics (of the diffusion process) are limited by the macroscopic presence of H-bonding dynamic crosslinks. The amount of H-bonding crosslinks is determined by the equilibrium constant K that defines the degree of H-bonding association. Although the van't Hoff relationship predicts that this equilibrium is also temperature dependent, the literature suggests that UPy H-bonding equilibrium is strongly in favor to association state, even at 120 °C.¹⁷ Therefore, while the presence of UPy H-bonding groups lowers the absolute value of diffusion coefficient, it does not change the activation energy in the same manner as it does for viscous relaxation. At higher temperatures, when K is on the order of unity, this situation may be different and the copolymer curves in Fig. 2 are expected to fall upon the unfunctionalized PBA curve. This may be the subject of a future study.

In conclusion, Multi-Photon Fluorescence Recovery After Photobleaching was demonstrated as an effective tool to study dye diffusion in reversibly associating polymer melts. This technique enables a side-by-side comparison of diffusion and viscous relaxation. Arrhenius plots of molecular diffusivity and shear viscosity indicate that association affects diffusion and viscous relaxation in fundamentally different ways: small molecule mass transport is determined by the fraction of associated dimers, whereas viscous relaxation is limited by the frequency of dissociation events. The reduction in mass diffusivity can be explained on the basis of reduced free volume: associating groups act like covalent crosslinks, lowering hole free volume that is available for mass transport. Density measurements confirm that copolymers containing associating groups exhibit higher densities. Thus, small molecule diffusion through associating polymers appears to be limited by thermal equilibrium, *i.e.* the value of the association constant K . On the other hand, viscous relaxation is limited by the kinetics of H-bonding dissociation, *i.e.* the value of the rate constant k_d .

Notes and references

1. G. Broze, R. Jerome and P. Teyssie, *Macromolecules*, 1981, **14**, 224-225.
2. R. P. Sijbesma, F. H. Beijer, L. Brunsveld, B. J. B. Folmer, J. H. K. K. Hirschberg, R. F. M. Lange, J. K. L. Lowe and E. W. Meijer, *Science*, 1997, **278**, 1601-1604.
3. J. Li, J. A. Viveros, M. H. Wrue and M. Anthamatten, *Advanced Materials*, 2007, **19**, 2851-2855.
4. K. Yamauchi, J. R. Lizotte and T. E. Long, *Macromolecules*, 2003, **36**, 1083-1088.
5. P. Cordier, F. Tournilhac, C. Soulie-Ziakovic and L. Leibler, *Nature*, 2008, **451**, 977-980.
6. S. Sivakova, D. A. Bohnsack, M. E. Mackay, P. Suwanmala and S. J. Rowan, *J. Am. Chem. Soc.*, 2005, **127**, 18202-18211.
7. M. J. Serpe, M. Rivera, F. R. Kersey, R. L. Clark and S. L. Craig, *Langmuir*, 2008, **24**, 4738-4742.
8. W. C. Yount, D. M. Loveless and S. L. Craig, *Angewandte Chemie-International Edition*, 2005, **44**, 2746-2748.
9. S. H. M. Soentjens, R. P. Sijbesma, M. H. P. van Genderen and E. W. Meijer, *J. Am. Chem. Soc.*, 2000, **122**, 7487-7495.
10. K. C. Tseng, N. J. Turro and C. J. Durning, *Polymer*, 2000, **41**, 4751-4755.
11. Y. Cheng, R. K. Prud'homme and J. L. Thomas, *Macromolecules*, 2002, **35**, 8111-8121.
12. E. Van Keuren and W. Schrof, *Macromolecules*, 2003, **36**, 5002-5007.
13. E. B. Brown, E. S. Wu, W. Zipfel and W. W. Webb, *Biophys J*, 1999, **77**, 2837-2849.
14. J. S. Vrentas and C. M. Vrentas, *Journal of Applied Polymer Science*, 1991, **42**, 1931-1937.
15. J. S. Vrentas, J. L. Duda and H. C. Ling, *J Polym Sci Pol Phys*, 1985, **23**, 275-288.
16. I. Barudio, G. Fevotte and T. F. McKenna, *Eur. Polym. J.*, 1999, **35**, 775-780.
17. D. J. M. van Beek, A. J. H. Spiering, G. W. M. Peters, K. te Nijenhuis and R. P. Sijbesma, *Macromolecules*, 2007, **40**, 8464-8475.

Heterogeneity of β -adrenergic receptor expression, signaling, and function in breast cancer cell lines

Kelley S. Madden^{*}, Mercedes J. Szpunar, Edward B. Brown
University of Rochester Medical Center, Rochester, NY

***Corresponding Author:**

Kelley S. Madden, Ph.D.
University of Rochester Medical Center
Department of Biomedical Engineering
Goergen Hall; RC Box 270168
Rochester, NY 14642
E-mail: Kelley_Madden@urmc.rochester.edu
Telephone: 585-273-5724
Fax: 585-276-2254

Co-authors:

Edward B. Brown, Ph.D.
University of Rochester Medical Center
Department of Biomedical Engineering
Goergen Hall; RC Box 270168
Rochester, NY 14642
E-mail: Edward_Brown@urmc.rochester.edu
Telephone: 585-273-5918
Fax: 585-276-2254

Mercedes J. Szpunar
Department of Pathology
University of Rochester Medical Center
601 Elmwood Ave.
Rochester, NY 14642
E-mail: Mercedes_Szpunar@urmc.rochester.edu
Telephone: 585-276-2254

Keywords:

Breast cancer, β -adrenergic receptors, proliferation, cAMP, VEGF

ABSTRACT

Introduction. β -adrenergic receptor (β -AR) stimulation drives proangiogenic factor production in several types of cancers. To examine the prevalence of this proangiogenic pathway in breast cancer cells, we analyzed a panel of seven human and murine breast cancer cell lines for β -AR cell surface expression, signaling capacity, and β -AR-mediated functional effects *in vitro*. **Methods and Results.** Specific binding of the β -AR radioligand [125 I]-cyanopindolol was used to determine β -AR expression and affinity. β -AR expression in these cell lines ranged from no detectable receptors to ~14,000 receptor sites per cell. To determine the efficiency of β -AR coupling to its intracellular signaling pathway, the rise in intracellular cAMP was measured after stimulation with the β -AR agonist isoproterenol (ISO). In 5 out of 7 cell lines, cAMP production correlated with β -AR expression, but in two of the cell lines that express β -AR, β -AR stimulation did not elicit increased intracellular cAMP. Differences in β -AR signaling capacity were not due to differences in adenylate cyclase activity, as direct activation of adenylate cyclase with forskolin did not elicit similar differences in cAMP production. In two high β -AR-expressing cells lines (MB-231 and MB-231BR, a brain-metastasizing MB-231 variant), the kinetics of β -AR-induced cAMP accumulation differed considerably. After 60 minutes of β -AR stimulation, cAMP declined to near baseline in MB-231BR, but was minimally reduced in MB-231. Functionally, ISO and the β_2 -AR-selective agonist terbutaline increased vascular endothelial growth factor (VEGF) production *in vitro* by MB-231BR, but β -AR stimulation did not alter VEGF production by MB-231 or MB-361, a low β -AR-expressing cell line. Furthermore, β -AR stimulation inhibited MB-361 cellular proliferation but did not alter MB-231BR or MB-231 proliferation *in vitro*. The ISO- and terbutaline-induced alterations in VEGF production and cell proliferation were blocked by a β_2 -AR-selective antagonist.

Conclusions. These results demonstrate that the number of β -AR expressed and the magnitude of the cAMP response following β -AR activation are not the sole determinants of functional responsiveness to β -AR stimulation. The heterogeneity of breast cancer cell responses to β -AR activation must be taken into account when considering β -AR as a potential therapeutic target for breast cancer treatment.

INTRODUCTION

In vivo studies in laboratory animals have demonstrated that the sympathetic nervous system can facilitate growth of solid tumors [1, 2], but the underlying mechanisms are only beginning to be elucidated. Several groups have demonstrated a role for β -adrenergic receptor (β -AR) activation in promoting solid tumor growth, angiogenesis, and metastases [1, 3, 4]. β -AR are G-protein coupled receptors that respond to norepinephrine and epinephrine by translocation of G-stimulator (G_s) subunit to activate adenylate cyclase and increase 3'-5'-cyclic adenosine monophosphate (cAMP) production. cAMP activates protein kinase A to elicit down-stream alterations in gene expression. Feedback inhibition of β -AR signaling is regulated by cyclic nucleotide phosphodiesterases and β -AR desensitization, and regulation of receptor desensitization plays an important role in disease processes and treatment, such as heart failure [5-7].

Several groups have recently provided evidence that direct stimulation of β -AR expressed by tumor cells themselves may play a role in tumor pathogenesis. Thaker and colleagues demonstrated that chronic stressor exposure augmented ovarian tumor growth in conjunction with increased tumor angiogenesis and elevated vascular endothelial growth factor (VEGF) [1]. The tumor growth-promoting effect was blocked by treatment with the β -AR antagonist propranolol. Importantly, this effect was eliminated in stressed animals implanted with the same line of ovarian tumor cells that had been altered so they were unable to express β -AR, implicating tumor cell β -AR expression and signaling in driving a proangiogenic pathway *in vivo*. *In vitro* studies suggest that this pathway may be active in other tumor cell types, such as ovarian and nasopharyngeal carcinoma and melanoma, and in normal cells, including cardiomyocytes, adipocytes, and mononuclear cells [4, 8-12].

We are interested in understanding the molecular basis underlying changes in breast cancer pathogenesis elicited through emotional or physical stressors. To develop a mouse model that mimics human breast cancer in terms of stress-induced changes in tumor pathogenesis, we needed to understand the level of heterogeneity in β -AR expression and signaling capacity within breast adenocarcinomas of mouse and human origin isolated from primary and secondary sites. We demonstrate that β -AR in human and murine breast tumor cell lines vary widely and stimulation of these receptors generally mirror β -AR signaling capacity as measured by elevated intracellular cAMP. However, neither β -AR expression nor peak cAMP signaling capacity was predictive of functional effects, i.e., VEGF production, *in vitro*. These results suggest that heterogeneity of β -AR signaling pathways utilized by breast cancer cells needs to be taken into account when considering β -blockade as a therapeutic strategy to inhibit angiogenesis in breast cancer.

METHODS & MATERIALS

Cell Lines. Human breast adenocarcinoma cell lines MDA-MB-231 (MB-231), MDA-MB-361 (MB-361), BT-474 and the mouse mammary tumor cell line 4T1 were purchased from American Tissue Type Collection (Manassas, VA). The murine mammary tumor cell line TG1-1 was obtained from Dr. R. K. Jain (Massachusetts General Hospital, Harvard Medical School, Boston, MA); MDA-MB-231BR, a brain-seeking variant of MB-231 was obtained from Dr. T. Yoneda (University of Texas Health Science Center, San Antonio, TX); and MCAIV was obtained from Dr. B. Fenton (University of Rochester, Rochester, NY). The characteristics of these cell lines, including hormone receptor expression and site from which the cells were isolated are described in Table 1. All cell lines except 4T1 were grown in Dulbecco's Modified Essential Medium

(DMEM) containing 4.5 g/L glucose, L-glutamine, penicillin/streptomycin and 10% fetal calf serum (FCS). 4T1 was grown in RPMI 1640 containing penicillin/streptomycin and 10% FCS. Cells were harvested by incubation with 0.25% trypsin + 0.05% EDTA for 3 minutes at 37°C. Ice-cold medium containing 10% FCS was used to stop the trypsin reaction. Cells were centrifuged at 200 x g at 4°C and resuspended in the appropriate medium. Cells were counted using a hemacytometer and Trypan blue to determine cell viability. All cells were grown in T75 tissue culture flasks (Corning Inc., Corning, NY) to no greater than 70-80% confluence.

Reagents. (-)Isoproterenol hydrochloride (ISO), terbutaline hemisulfate (TERB), isobutylmethylxanthine (IBMX), and forskolin were purchased from Sigma-Aldrich, St. Louis, MO. [¹²⁵I]-cyanopindolol (¹²⁵ICYP) was purchased from NEN Radiochemicals (Perkin Elmer Life and Analytical Sciences, Waltham, MA). All media, Hank's Balanced Salt Solution (HBSS) and components were purchased from Gibco, Invitrogen Inc., Carlsbad, CA.

β-AR Radioligand Binding Assay. The specific binding of ¹²⁵ICYP to whole cells was used to quantify β-AR expression [13]. Tumor cells (1x10⁶) resuspended in HBSS were incubated with varying concentrations of ¹²⁵ICYP with or without the unlabeled β-AR-antagonist CGP-12177 (1 μM) in duplicate tubes. Incubations were carried out in 13 x 100-mm polypropylene tubes for 60 minutes in a shaking water bath at 37°C. This is sufficient time for equilibrium binding to occur. Following incubation, 3 ml of ice-cold hypotonic phosphate buffer (3.8 mM KH₂O₄, 16.2 mM Na₂HPO₄, and 4 mM MgSO₄) was added to each tube, and the tubes were incubated for 10 minutes on ice. The reaction mixtures were filtered under reduced pressure through Whatman glass fiber filters using an automatic harvester (Brandel Corp., Gaithersburg, MD). Filters were

rinsed with 16 ml of ice-cold Tris-EGTA buffer to remove unbound radioligand, transferred to 12 x 75 mm glass tubes, and radioactivity was determined in a LKB Clinigamma gamma counter. Specific binding is defined as the difference between binding of the radioligand at each concentration in the absence and in the presence of 1 μ M CGP-12177, and was calculated for each ligand concentration using the specific activity of the radioligand. For each experimental repetition, specific 125 ICYP (M) bound versus the amount of ligand added was plotted, and the maximal number of binding sites (B_{\max}) and receptor affinity (Kd) was determined using non-linear regression analysis (GraphPad Prism software; San Diego, CA). The maximal number of binding sites per cell is calculated from the B_{\max} based on simple stoichiometric assumptions (one molecule binds to one receptor site).

cAMP Assay. Tumor cells (1×10^6) in 12 x 75 mm polypropylene tubes were incubated for 20 minutes at 37°C in a shaking water bath in HBSS containing 0.1% bovine serum albumin (BSA) and 100 μ M isobutylmethylxanthine (IBMX), a phosphodiesterase inhibitor (HBSS/BSA/IBMX buffer). Adrenergic agonist of varying concentrations or forskolin or buffer alone was added to each tube and the cells were incubated for 5-60 minutes at 37°C (final volume = 1 ml). To stop the reaction, 2 ml ice-cold HBSS/BSA/IBMX buffer was added to each tube. The cells were centrifuged two times for 10 minutes at 200 x g and then resuspended in Cell Lysis Buffer, provided 5X in the cAMP ELISA kit and diluted to 1X with dH₂O prior to use. Intracellular cAMP was released by subjecting the cells to freezing at -20°C, followed by boiling for 10 minutes in a 95°C heat block and repeating the sequence. After centrifugation at 600 x g at 4°C for 10 minutes to remove cellular debris, the supernatants were collected and stored at -80°C until analysis of cAMP content using the cAMP Parameter ELISA kit from R & D Systems

(Minneapolis, MN) following the manufacturer's instructions. For each supernatant at least two supernatant dilutions were tested to determine the optimal dilution. Absorption was measured at 450 nm using a multiwell plate reader (Synergy HT, Biotek Instruments Inc, Winooski, VT). Non-specific binding (binding in the absence of the primary anti-cAMP antibody) was automatically subtracted from all wells. Curve fitting and sample concentration calculations were conducted with Gen5 software (Biotek). Results are expressed as pmoles/mL /10⁶ cells.

Cellular Proliferation *in vitro*. Tumor cells were resuspended in Advanced DMEM containing 1% FCS, penicillin/streptomycin, and L-glutamax (Invitrogen) and plated at 1-2 x10⁴ cells per well in 96-well flat bottom tissue culture plates (Falcon, Becton Dickinson, Franklin Lakes, NJ) in triplicate, and allowed to adhere for 3 hours at 37°C in a 5% CO₂ humidified atmosphere before addition of adrenergic agonists or antagonists. For blocking experiments, antagonists were added 30 minutes prior to addition of agonists. Proliferation was measured using a fluorescent DNA binding dye (CyQuant NF Proliferation Assay kit, Invitrogen) according to manufacturer's instructions. Fluorescent intensity was measured at excitation 490 nm and emission 520 nm using a multiwell plate reader equipped with the appropriate filters. Background fluorescence (in the absence of cells) was subtracted automatically from each well.

VEGF Production *in vitro*. Tumor cells were resuspended in Advanced DMEM containing 1% FCS, penicillin/streptomycin, and L-glutamax (Invitrogen). Cells were plated at 5x10⁴ cells per well in 12-well flat bottom tissue culture plates (Falcon, Becton Dickinson). At this concentration, tumor cells reached confluence by 96 hours in culture. Cells were allowed to adhere for 3 hours at 37°C before addition of adrenergic agonists or antagonists. Supernatants

were harvested at 48, 72, and 96 hours of culture at 37°C in 5% CO₂ humidified atmosphere.

VEGF concentration in cell-free supernatants was measured using a human VEGF Quantikine kit (R&D Systems). Absorption was measured at 450 nm using a multiwell plate reader.

Background (absorbance in the absence of the primary anti-VEGF antibody) was automatically subtracted from all wells. Curve fitting and sample concentration calculations were conducted with Gen5 software.

Statistical Analysis. Significant differences between groups were determined using one- or two-way analysis of variance (ANOVA) using GraphPad Prism software. When significant main effects or interactions were identified ($p < 0.05$), Newman-Keuls or Bonferroni's post-hoc tests, respectively, were used for multiple-group comparisons. A p -value < 0.05 is considered statistically significant.

RESULTS

I. β -AR expression and signaling capacity varies between breast cancer cell lines

To initiate experiments designed to examine stress-induced alterations in breast tumor growth, we wanted to identify breast cancer cell lines that exhibit high sensitivity to β -AR activation. Therefore, we screened a panel of murine and human breast cancer cell lines for β -AR expression and signaling. To quantify β -AR cell surface expression, we measured the binding of the β -AR non-selective antagonist ¹²⁵ICYP to whole cells. Specificity was determined by measuring radioligand binding in the presence or absence of the unlabeled β -AR antagonist CGP-12177. Specific ¹²⁵ICYP binding was detected in all breast cancer cell lines except in the mouse line 4T1, which displayed no specific binding (Fig. 1A). High levels of specific binding

were observed in MB-231 (Fig. 1B) and MB-231BR (Fig. 1C) compared to the other cell lines (Fig. 1F). The mouse line TG1-1 displayed intermediate levels of specific binding (Fig. 1F), and the mouse line MCalV (Fig. 1D) and human lines MB-361 (Fig. 1E) and BT-474 (Fig. 1F) displayed very low specific binding. The affinity of binding (K_d) for all β -AR-expressing cell lines ranged from 1×10^{-10} to 7×10^{-10} M. β -AR expression could be rank ordered based on the average number sites per cell: MB231 ($13,798 \pm 4,858$) = MB-231BR ($11,027 \pm 3,991$) > TG1-1 ($2,793 \pm 543$) > MCalV (721 ± 54) > BT-474 (232) = MB361 (160) > 4T1 (not detectable).

Based on β -AR expression, we expected significant variation in β -AR signaling capacity, as measured by β -agonist-induced intracellular cAMP. In Fig. 2, cAMP production was measured in the presence of the phosphodiesterase inhibitor IBMX to prevent hydrolysis of cAMP and to minimize the possibility that variation in phosphodiesterase activity contributed to differences in β -AR-induced intracellular cAMP. Peak cAMP accumulation was measured 5 minutes after stimulation with 10^{-4} M ISO, a non-selective β -AR agonist (Fig. 2A). ISO elicited the highest level of cAMP in MB-231 compared to all cell lines. Although MB-231 and MB-231BR expressed similar numbers of β -AR per cell, MB-231BR cAMP was lower than MB-231 but higher than the remaining cell lines. TG1-1 was intermediate in cAMP production, and MB-361 increased cAMP moderately. In 4T1, basal cAMP was higher compared to all other cell lines, and cAMP was not elevated significantly above baseline in response to ISO, consistent with the inability to detect specific radioligand binding in this cell line. Although MCalV and BT-474 expressed low, but detectable levels of β -AR (Fig. 1F), neither MCalV (Fig. 2A) nor BT-474 (data not shown) produced cAMP significantly above the level of detection.

II. Heterogeneity of adenylate cyclase activity

Altered adenylate cyclase activity could be responsible for differences in ISO-induced cAMP production between these cell lines. For example, the inability of MCaIV and BT-474 to produce cAMP despite expression of β -AR expression could be explained by impaired adenylate cyclase. To by-pass β -AR coupling to adenylate cyclase, we stimulated cells with forskolin, a direct activator of adenylate cyclase (Fig. 2B). Forskolin produced more cAMP in MB-231BR compared to MB-231, and TG1-1 was poorly stimulated compared to all cell lines tested, while 4T1 was exquisitely sensitive to forskolin. Forskolin elicited high levels of cAMP in MCaIV cells, equivalent to that of MB-231BR, demonstrating that the defect in β -AR signaling in MCaIV cells is not related to a deficit in adenylate cyclase activity. In contrast, forskolin did not increase cAMP in BT-474 (data not shown). (The response of MB-361 to forskolin was not tested.) Thus, cAMP elevation following direct adenylate cyclase stimulation varies from cell line to cell line, but this heterogeneity does not correlate with the differences in β -AR signaling.

III. Kinetics of β -AR-induced cAMP production

We next determined if the heterogeneity of the peak cAMP response to β -AR stimulation extends to the kinetics of the cAMP response. The kinetics of the cAMP response is a function of the rate of cAMP accumulation – which is a reflection of the number of β -AR, the efficiency of β -AR coupling to adenylate cyclase, and the rate of at which the response is turned off by receptor desensitization. We noted the discrepancy between β -AR expression and β -AR-induced peak cAMP production between the two high β -AR-expressing cell lines MB-231 and MB-231BR and postulated that differences in the kinetics of the cAMP response may contribute to this difference. We also tested the low β -AR-expressing cell line MB-361 to determine how cAMP kinetics is influenced by the overall magnitude of the peak cAMP response. We stimulated the cells with ISO in the presence of IBMX, so that a decline in the response could be

attributed to receptor desensitization and not to phosphodiesterase hydrolysis of cAMP. In MB-361, peak cAMP accumulation occurred 5 minutes after addition of either 10^{-5} M or 10^{-4} M ISO, followed by a gradual decline in cAMP to near baseline by 60 minutes (Fig. 3A). In these cells, the response to 10^{-6} M ISO plateaued at 20 and 60 minutes at a level of cAMP that was barely above the level of detection of the assay. Similar cAMP kinetics were observed in MB-231BR, which produced a rapid rise and decline in intracellular cAMP after stimulation with all concentrations of ISO tested (Fig. 3B). Additionally, these cells were more sensitive to β -AR stimulation than MB-361, as a rapid, detectable rise in cAMP was detected at 10^{-7} M ISO that was higher in magnitude than the MB-361 response to 10^{-6} M ISO. In MB-231, the magnitude and the kinetics of the cAMP response differ considerably compared to that of MB-231BR and MB-361 (Fig. 3C). Most strikingly, cAMP decreased either slightly or not at all within the 60 minute time period at a wide range of ISO concentrations tested. MB-231 was very sensitive to β -AR-induced stimulation, with the cAMP response to 10^{-7} M and 10^{-6} M ISO remaining above 100 pmol/mL for at least 60 minutes. These results suggest that the number of β -AR influences the magnitude of the peak cAMP accumulation. However, the kinetics of the cAMP response suggests differences in the molecular mechanisms that down-regulate the cAMP response.

IV. Functional consequences of β -AR signaling of breast cancer cells in vitro

We next determined if the observed heterogeneity in β -AR signaling mirrored differences in the functional response to β -AR stimulation. Since several recent reports have suggested that β -AR activation of tumor cells *in vitro* promotes a proangiogenic pathway featuring increased VEGF [4, 9, 12], we asked if β -AR stimulation increased VEGF production by MB-231, MB-231BR, and MB-361 *in vitro*. ISO stimulation of MB-231BR elevated VEGF production from 48 to 96 hours in culture (Fig. 4A; two-way repeated measures ANOVA; main effect of ISO,

$p < 0.0001$), with statistically significant increases as assessed by Bonferroni's post-test analysis achieved at 72 and 96 hours in culture. For MB-231 and MB-361, no significant differences in VEGF production were observed in the presence of 1 or 10 μM ISO at any time point (Fig. 4B, C; two-way repeated measures ANOVA; $p > 0.05$). To probe the sensitivity of MB-231BR to β -AR stimulation, dose response curves to ISO and the β_2 -AR-selective agonist terbutaline were compared. At 10^{-7} M ISO, a slight non-statistical enhancement of VEGF was achieved (Fig. 5A; one-way ANOVA, main effect of treatment, $p = 0.002$). Increased VEGF production was observed at concentrations as low as 10^{-8} M with the β_2 -selective agonist terbutaline (Fig. 5B; one-way ANOVA, main effect of treatment, $p < 0.0001$). To determine if the ISO-induced enhancement in VEGF production by MB-231BR was β -AR-mediated, the non-selective β -AR antagonist nadolol was used to block ISO activation of β -AR. Nadolol completely inhibited the ISO-induced increase in MB-231BR VEGF production (Fig. 5C; one-way ANOVA, main effect of treatment, $p = 0.005$). The β_2 -AR-selective blocker ICI 118,551 also completely prevented the ISO-induced VEGF enhancement suggesting β_2 -AR involvement in enhanced VEGF production in this cell line (Fig. 5D; one-way ANOVA, main effect of treatment, $p = 0.003$).

β -AR receptor signaling has been reported to alter proliferation of breast cancer cell lines *in vitro*, including MB-231 [14]. To determine if β -AR signaling altered tumor cell proliferation and to determine if the ISO-induced changes in VEGF production are a function of altered cell number, we measured proliferation at varying time points in culture. Neither MB-231BR (Fig. 6A) or MB-231 (data not shown) proliferation was significantly altered by ISO, but ISO significantly reduced proliferation of MB-361 cells (Fig. 6B; two-way ANOVA, main effect of ISO treatment, $p = .03$). The results in Fig. 6B show inhibition at 72 hours in culture, but ISO

also inhibited proliferation in MB-361 at 48 and 96 hours in culture (data not shown). The ISO-induced decrease in proliferation was blocked by the β -AR non-selective antagonist nadolol and ICI-118,551 (Fig. 6B). Furthermore, terbutaline inhibited MB-361 proliferation and the effect was blocked by the β_2 -AR-selective blocker ICI 115,881 (Fig. 6C; one-way ANOVA, main effect, $p=0.006$), suggesting that MB-361 stimulation of β_2 -AR is responsible for decreased proliferation. Cellular proliferation was not significantly altered by β -AR activation in MB-231, TG1-1, MCalV, BT-474 or 4T1 (data not shown). Together, these results demonstrate that the β -AR elevation of VEGF production in MB-231BR is independent of altered cellular proliferation, and β -AR stimulation directly elicits changes in VEGF production or proliferation in only certain breast cancer cell lines.

DISCUSSION

In breast cancer, characterization of estrogen receptors, progesterone receptors, and HER2/neu expression in breast cancer has led to more effective, individualized treatment regimens [15]. We have demonstrated that phenotypic heterogeneity within breast cancer can be extended to β -AR, whose endogenous ligands norepinephrine and epinephrine are released following activation of the sympathetic nervous system. Using radioligand binding to quantify β -AR expression, a wide range of specific radioligand binding was observed. β -AR signaling capacity as measured by accumulated intracellular cAMP was not always predicted by β -AR expression. In turn, β -AR-induced alterations in VEGF production or cellular proliferation were not predicated on the magnitude of β -AR-induced cAMP accumulation. Together, these results suggest that unlike the situation with hormone receptors, simply measuring β -AR expression is not sufficient to determine therapeutic outcome.

I. β -AR coupling to adenylate cyclase

β -AR expression correlating with the cAMP response to β -AR stimulation suggests efficient interactions between β -AR, G_s and adenylate cyclase. Such a relationship was observed with the two high- β -AR expressing cell lines MB-231 and MB-231BR as well as the low β -AR expressing MB-361. In MCAIV and BT-474, however, β -AR expression did not translate into significant β -AR-induced accumulation of cAMP above the limits of detection of the ELISA. Direct activation of adenylate cyclase with forskolin was used to determine if the inability to respond to β -AR stimulation was due to a global defect in adenylate cyclase. Forskolin-induced cAMP levels in MCAIV were equivalent to that of MB-231BR, a good responder to forskolin. This result implies that β -AR coupling to adenylate cyclase is impaired in MCAIV. On the other hand, BT-474 did not respond to forskolin (data not shown), suggesting a deficiency in adenylate

cyclase that may contribute to the lack of β -AR signaling in this cell line. BT-474 was isolated from a solid, invasive ductal carcinoma of the breast and is the only human adenocarcinoma derived directly from the breast that we tested [16]; the other human breast cancer cell lines were derived from secondary sites. Therefore, β -AR expression, signaling, and function in primary human breast tumors require further investigation.

In the remaining cell lines, we noted differences in the response to forskolin that were not mirrored in the differences in β -AR receptor-specific signaling. For example, TG1-1, a cell line with intermediate β -AR expression and β -AR-induced cAMP production, had a relatively poor response to direct adenylate cyclase activation with forskolin. The relatively high cAMP response to β -AR stimulation in TG1-1 suggests a high efficiency of β -AR-coupling to adenylate cyclase in these cells. The response of 4T1 to forskolin was the highest of all the cell lines tested here. This sensitivity to forskolin may indicate increased adenylate cyclase activity that may contribute to the elevated basal levels of cAMP noted in this cell line. The heterogeneity of forskolin responsiveness demonstrates signaling heterogeneity at the level of adenylate cyclase in breast cancer cell lines, but the efficiency of β -AR ligand-induced coupling to adenylate cyclase may be impaired or enhanced independently of global adenylate cyclase activity.

II. β -AR signaling does not correlate with function *in vitro*

β -AR signaling capacity as measured by the magnitude of cAMP accumulation did not predict the functional response to β -AR stimulation as measured by VEGF production. ISO concentrations from 10^{-9} M (data not shown) to 10^{-5} M did not alter VEGF production by MB-361, a low β -AR-expressing line, or MB-231, a high β -AR-expressing cell line. By contrast, in MB-231BR, a high β -AR-expressing cell line, β -AR stimulation enhanced VEGF production at concentrations of the selective β_2 -AR agonist terbutaline as low as 10^{-8} M and with the non-

selective agonist ISO as low as 10^{-7} M. A β_2 -AR-selective antagonist blocked the ISO-induced increase in VEGF, confirming that the increase in VEGF production is mediated by β_2 -AR. In normal cells, the β -AR/adenylate cyclase/cAMP system is tightly controlled and employs negative regulators to fine-tune signal transduction output [6, 17]. In MB-231, the high level of cAMP accumulation and the prolonged duration of the response relative to MB-231BR and MB-361 is evidence that feedback mechanisms may be impaired in MB-231. An impaired ability to regulate cAMP may lead to inhibition of down-stream effector systems that lead to increased production of VEGF in MB-231BR. This possibility is an active area of research in our laboratory.

Finally, the enhanced production of VEGF in MB-231BR was not due to a β -AR-induced increase in cell number, as proliferation was not increased in the presence of ISO. Other investigators have shown reduced MB-231 proliferation with exposure to β -AR agonists *in vitro* [14]. In our hands, MB-231 proliferation was inhibited 10-15% at the highest concentration of ISO tested (10^{-5} M), but this effect was not statistically significant and could not be blocked by β -blockers (data not shown). MB-361 proliferation was inhibited in the presence of ISO and terbutaline. The ISO- and terbutaline-induced inhibition of proliferation MB-361 was blocked by nadolol and the β_2 -selective antagonist ICI 118, 551. We tested MB-361 in part because it was derived from a human brain metastasis while MB-231BR was derived by isolating MB-231 variants that migrated to the brain in nude mice [18-20]. MB-361 exhibited very low β -AR expression and correspondingly low cAMP response to ISO; hence it is apparent that the high β -AR expression in MB-231BR is not a general feature of breast adenocarcinomas isolated from the brain.

III. Potential *in vivo* β -AR signaling in breast tumor pathogenesis

Thaker and colleagues showed increased VEGF in MB-231 tumors growing orthotopically in the mammary fat pad following chronic stressor exposure [1]. Our inability to demonstrate effects of β -AR stimulation of MB-231 *in vitro* suggests that β -AR-induced VEGF production by MB-231 tumors *in vivo* may be facilitated by interactions with β -AR-expressing cells of the tumor stroma. Furthermore, upon exposure to β -AR agonists *in vitro* myeloma and nasopharyngeal cell lines increased production of VEGF and other proangiogenic molecules, including matrix metalloproteinases-2 and -9 [4, 9]. Under our culture conditions production of these matrix metalloproteinases by MB-231 and MB-231BR was not detectable with or without ISO (data not shown). Given the ubiquity of β -AR expression in normal fibroblasts, endothelial cells, and cells of the immune system [21-25], it is also likely that stromal cells, the non-tumor host cells present within the tumor, contribute to β -AR-induced changes in tumor pathogenesis to up-regulate proangiogenic factors *in vivo*.

IV. Conclusions

β -AR augmentation of a proangiogenic pathway has recently been demonstrated in tumor cell lines derived from several different types of solid cancers, including breast cancer. The existence of a β -AR-driven proangiogenic pathway suggests that β -AR blockade, commonly used in the treatment of cardiovascular disease, may be effective at blocking undesirable stress effects if used in conjunction with other anti-angiogenic therapies in breast cancer patients. In order to pursue β -AR blockade as a therapeutic option, it is important to understand the ubiquity of β -AR expression, signaling and function in breast tumors. We have demonstrated a wide degree of heterogeneity in β -AR expression and functional effects in the breast tumor cell lines tested here. Furthermore, β -AR-induced VEGF production is prominent only in MB-231BR, a human breast cancer cell line that preferentially metastasizes to the brain in mouse models. Our

results also demonstrate that neither β -AR receptor expression nor the peak magnitude of β -AR-induced cAMP accumulation are good predictors of the functional impact of β -AR activation in these breast cancer cell lines. Our goal is to identify the down-stream effectors that elicit increased proangiogenic factor production and to determine the mechanism underlying the apparent lack of a β -AR-induced functional response in MB-231 compared to MB-231BR so that more accurate predictions can be made regarding responsiveness of breast cancer cells to β -AR stimulation. Our results imply that the outcome of direct stimulation of β -AR on breast tumor cells in the context of a stressor will vary considerably from individual to individual. MB-231BR tumors may be more susceptible to stress-induced, catecholamine-mediated alterations in growth and/or metastasis – a hypothesis we are currently testing. Future studies will also determine if elevated β -AR expression and signaling contribute to the propensity of MB-231BR to enter the brain.

List of Abbreviations Used

β-AR: beta-adrenergic receptor(s)

cAMP: 3'-5'-cyclic adenosine monophosphate

HBSS: Hank's Balanced Salt Solution

BSA: bovine serum albumin

FCS: fetal calf serum

IBMX: isobutylmethylxanthine

ICI: ICI 118,551 hydrochloride

¹²⁵ICYP: ¹²⁵I-cyanopindolol

ISO: isoproterenol

NAD: nadolol

TERB: terbutaline

VEGF: vascular endothelial growth factor

ANOVA: Analysis of Variance

Competing Interests: The authors declare no competing interests.

Authors' Contributions:

KSM conceived, designed, and coordinated all experiments, conducted proliferation and radioligand binding experiments, analyzed and interpreted the results, and drafted the manuscript. MJS participated in design, analysis and interpretation of the VEGF experiments, and participated in the drafting of the manuscript. EBB conceived the experiments, interpreted the data, and helped draft the manuscript. All authors read and approved the final manuscript.

Acknowledgments. This work was supported by the Breast Cancer Coalition of Rochester to KSM, Department of Defense Era of Hope Scholar Award and Pew Scholar in the Biomedical Sciences Award to EBB, and a University of Rochester Clinical and Translational Science Institute training award to MJS. We thank Khawarl Liverpool, Michael Storonsky, and Tara Spencer for their excellent technical assistance.

References

1. Thaker PH, Han LY, Kamat AA, Arevalo JM, Takahashi R, Lu C, Jennings NB, Armaiz-Pena G, Bankson JA, Ravoori M *et al*: **Chronic stress promotes tumor growth and angiogenesis in a mouse model of ovarian carcinoma.** *Nat Med* 2006, **12**(8):939-944.
2. Raju B, Haug SR, Ibrahim SO, Heyeraas KJ: **Sympathectomy decreases size and invasiveness of tongue cancer in rats.** *Neuroscience* 2007, **149**(3):715-725.
3. Ben-Eliyahu S, Shakhar G, Page GG, Stefanski V, Shakhar K: **Suppression of NK cell activity and of resistance to metastasis by stress: a role for adrenal catecholamines and beta-adrenoceptors.** *Neuroimmunomodulation* 2000, **8**:154-164.
4. Yang EV, Sood AK, Chen M, Li Y, Eubank TD, Marsh CB, Jewell S, Flavahan NA, Morrison C, Yeh PE *et al*: **Norepinephrine up-regulates the expression of vascular endothelial growth factor, matrix metalloproteinase (MMP)-2, and MMP-9 in nasopharyngeal carcinoma tumor cells.** *Cancer research* 2006, **66**(21):10357-10364.
5. Lohse MJ, Engelhardt S, Eschenhagen T: **What is the role of beta-adrenergic signaling in heart failure?** *Circ Res* 2003, **93**(10):896-906.
6. Kohout TA, Lefkowitz RJ: **Regulation of G protein-coupled receptor kinases and arrestins during receptor desensitization.** *Molecular pharmacology* 2003, **63**(1):9-18.

7. Liggett SB, Cresci S, Kelly RJ, Syed FM, Matkovich SJ, Hahn HS, Diwan A, Martini JS, Sparks L, Parekh RR *et al*: **A GRK5 polymorphism that inhibits beta-adrenergic receptor signaling is protective in heart failure.** *Nat Med* 2008, **14**(5):510-517.
8. Weil J, Benndorf R, Fredersdorf S, Griesse DP, Eschenhagen T: **Norepinephrine upregulates vascular endothelial growth factor in rat cardiac myocytes by a paracrine mechanism.** *Angiogenesis* 2003, **6**(4):303-309.
9. Yang EV, Kim SJ, Donovan EL, Chen M, Gross AC, Webster Marketon JJ, Barsky SH, Glaser R: **Norepinephrine upregulates VEGF, IL-8, and IL-6 expression in human melanoma tumor cell lines: implications for stress-related enhancement of tumor progression.** *Brain Behav Immun* 2009, **23**(2):267-275.
10. Fredriksson JM, Lindquist JM, Bronnikov GE, Nedergaard J: **Norepinephrine induces vascular endothelial growth factor gene expression in brown adipocytes through a beta -adrenoreceptor/cAMP/protein kinase A pathway involving Src but independently of Erk1/2.** *J Biol Chem* 2000, **275**(18):13802-13811.
11. Banfi C, Cavalca V, Veglia F, Brioschi M, Barcella S, Mussoni L, Boccotti L, Tremoli E, Biglioli P, Agostoni P: **Neurohormonal activation is associated with increased levels of plasma matrix metalloproteinase-2 in human heart failure.** *European heart journal* 2005, **26**(5):481-488.
12. Lutgendorf SK, Cole S, Costanzo E, Bradley S, Coffin J, Jabbari S, Rainwater K, Ritchie JM, Yang M, Sood AK: **Stress-related mediators stimulate vascular**

- endothelial growth factor secretion by two ovarian cancer cell lines.** *Clin Cancer Res* 2003, **9**(12):4514-4521.
13. Engel G, Hoyer D, Berthold R, Wagner H: **(±)[125Iodo]cyanopindolol, a new ligand for β -adrenoceptors: Identification and quantification of subclasses of β -adrenoceptors in guinea pig.** *Naun Schmiedebergs ArchPharmacol* 1981, **317**:277-285.
 14. Slotkin TA, Zhang J, Dancel R, Garcia SJ, Willis C, Seidler FJ: **Beta-adrenoceptor signaling and its control of cell replication in MDA-MB-231 human breast cancer cells.** *Breast cancer research and treatment* 2000, **60**(2):153-166.
 15. Olopade OI, Grushko TA, Nanda R, Huo D: **Advances in breast cancer: pathways to personalized medicine.** *Clin Cancer Res* 2008, **14**(24):7988-7999.
 16. Lasfargues EY, Coutinho WG, Redfield ES: **Isolation of two human tumor epithelial cell lines from solid breast carcinomas.** *J Natl Cancer Inst* 1978, **61**(4):967-978.
 17. Xin W, Tran TM, Richter W, Clark RB, Rich TC: **Roles of GRK and PDE4 activities in the regulation of beta2 adrenergic signaling.** *The Journal of general physiology* 2008, **131**(4):349-364.
 18. Palmieri D, Bronder JL, Herring JM, Yoneda T, Weil RJ, Stark AM, Kurek R, Vega-Valle E, Feigenbaum L, Halverson D *et al*: **Her-2 overexpression increases the metastatic outgrowth of breast cancer cells in the brain.** *Cancer research* 2007, **67**(9):4190-4198.

19. Moasser MM, Basso A, Averbuch SD, Rosen N: **The tyrosine kinase inhibitor ZD1839 ("Iressa") inhibits HER2-driven signaling and suppresses the growth of HER2-overexpressing tumor cells.** *Cancer research* 2001, **61**(19):7184-7188.
20. Yoneda T, Williams PJ, Hiraga T, Niewolna M, Nishimura R: **A bone-seeking clone exhibits different biological properties from the MDA-MB-231 parental human breast cancer cells and a brain-seeking clone in vivo and in vitro.** *J Bone Miner Res* 2001, **16**(8):1486-1495.
21. Seya Y, Fukuda T, Isobe K, Kawakami Y, Takekoshi K: **Effect of norepinephrine on RhoA, MAP kinase, proliferation and VEGF expression in human umbilical vein endothelial cells.** *Eur J Pharmacol* 2006, **553**(1-3):54-60.
22. Kalinichenko VV, Mokyr MB, Graf LH, Jr., Cohen RL, Chambers DA: **Norepinephrine-mediated inhibition of antitumor cytotoxic T lymphocyte generation involves a β -adrenergic receptor mechanism and decreased TNF- α gene expression.** *Journal of Immunology* 1999, **163**:2492-2499.
23. Shakhar G, Ben-Eliyahu S: **In vivo β -adrenergic stimulation suppresses natural killer activity and compromises resistance to tumor metastasis in rats.** *Journal of Immunology* 1998, **160**:3251-3258.
24. Spengler RN, Chensue SW, Giacherio DA, Blenk N, Kunkel SL: **Endogenous norepinephrine regulates tumor necrosis factor-alpha production from macrophages in vitro.** *J Immunol* 1994, **152**(6):3024-3031.

25. Pullar CE, Isseroff RR: **Beta 2-adrenergic receptor activation delays dermal fibroblast-mediated contraction of collagen gels via a cAMP-dependent mechanism.** *Wound Repair Regen* 2005, **13**(4):405-411.
26. Aguilar Z, Akita RW, Finn RS, Ramos BL, Pegram MD, Kabbinavar FF, Pietras RJ, Pisacane P, Sliwkowski MX, Slamon DJ: **Biologic effects of heregulin/neu differentiation factor on normal and malignant human breast and ovarian epithelial cells.** *Oncogene* 1999, **18**(44):6050-6062.
27. Aslakson CJ, Miller FR: **Selective events in the metastatic process defined by analysis of the sequential dissemination of subpopulations of a mouse mammary tumor.** *Cancer research* 1992, **52**(6):1399-1405.
28. Chen Y, Hu D, Eling DJ, Robbins J, Kipps TJ: **DNA vaccines encoding full-length or truncated Neu induce protective immunity against Neu-expressing mammary tumors.** *Cancer research* 1998, **58**(9):1965-1971.
29. Suit HD, Sedlacek RS, Zietman A: **Quantitative transplantation assays of spontaneous tumors of the C3H mouse as allografts in athymic NCr/Sed-nu/nu nude mice and isografts in C3Hf/Sed mice.** *Cancer research* 1988, **48**(16):4525-4528.

Figure Legends

Fig. 1. Heterogeneity of β -AR expression in breast cancer cell lines. Binding of the radiolabeled β -AR antagonist ^{125}I CYP was measured in (A) 4T1, (B) MB-231, (C) MB-231BR, (D) MCalV, and (E) MB-361. Specific binding (solid line) at each ligand concentration was calculated by subtracting radioligand binding in the presence of unlabeled antagonist CGP-12177 from total ICYP binding. (F) The concentration of ^{125}I -CYP specifically bound at varying concentrations of ligand was calculated for each cell line as described in the methods. All binding curves were fit to a 3rd order polynomial equation. Results are representative of 2-3 experimental repetitions.

Fig. 2. Heterogeneity of cAMP response to β -AR and adenylate cyclase stimulation in breast cancer cell lines. cAMP production was measured after stimulation with (A) 0 ISO or 10^{-4} M ISO (5 minutes) or (B) 10^{-4} M forskolin (20 minutes). All reactions took place in the presence of 100 μM IBMX. cAMP was determined by ELISA. Results shown are mean \pm SEM of 1-4 experimental repetitions. n.d. = not detectable; the level of detection is 1 pmol/mL.

Fig. 3. Kinetics of cAMP production with β -AR activation. Varying concentrations of ISO were added to (A) MB-231, (B) MB-231BR, and (C) MB-361 in the presence of IBMX for varying periods of time. Intracellular cAMP concentration was determined by ELISA. Results shown are mean \pm SEM of 1-5 experimental repetitions.

Fig. 4. β -AR activation and VEGF production *in vitro*. ISO at varying doses was added to (A) MB-231BR, (B) MB-231, and (C) MB-361. Cell-free supernatant was harvested at varying time points, and VEGF content was determined by ELISA. Number of experimental repetitions: MB-

231, n=3; MB231BR, n=3; MDA-MB-361, n=3. Asterisks indicate statistically significant versus 0 ISO at each time point in culture by Bonferroni post-hoc analysis ($p<0.05$).

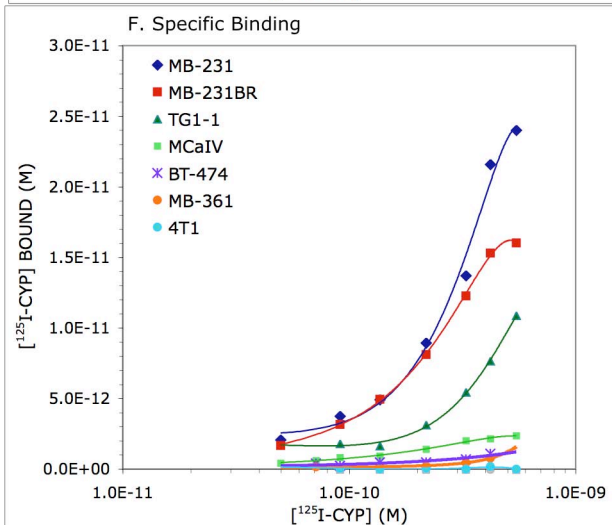
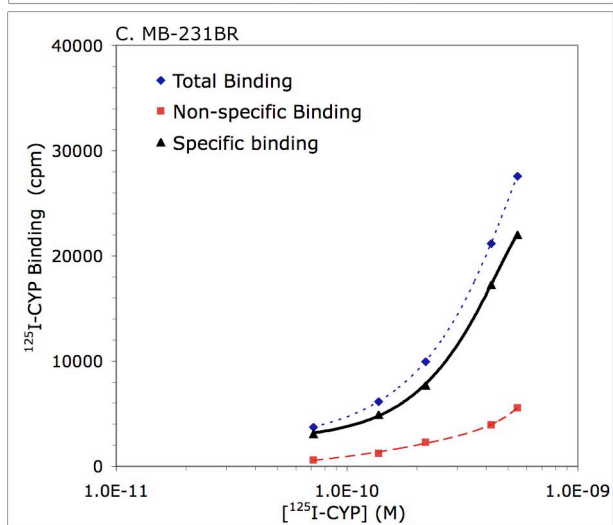
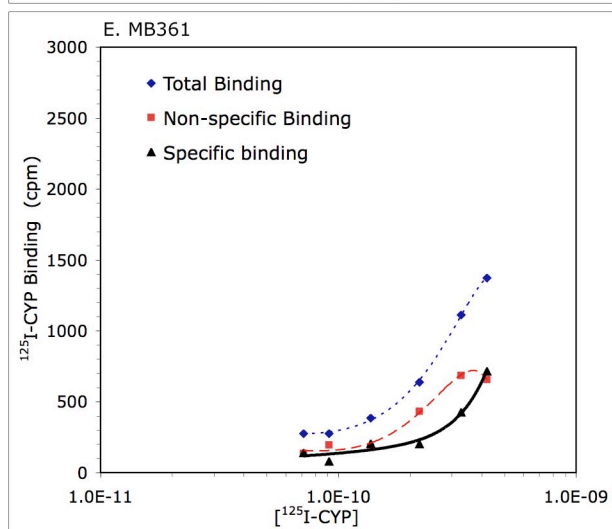
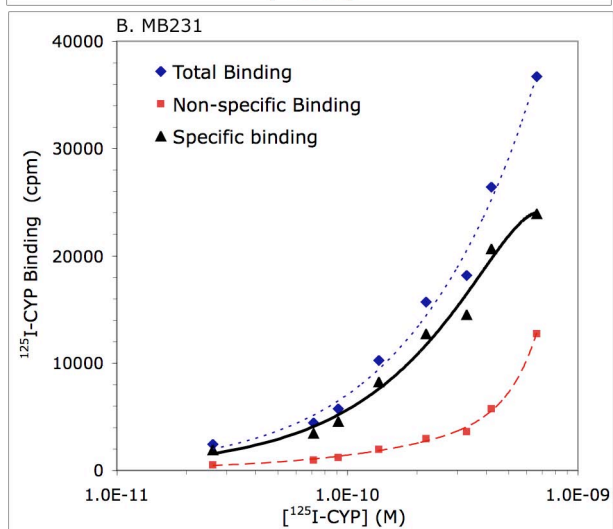
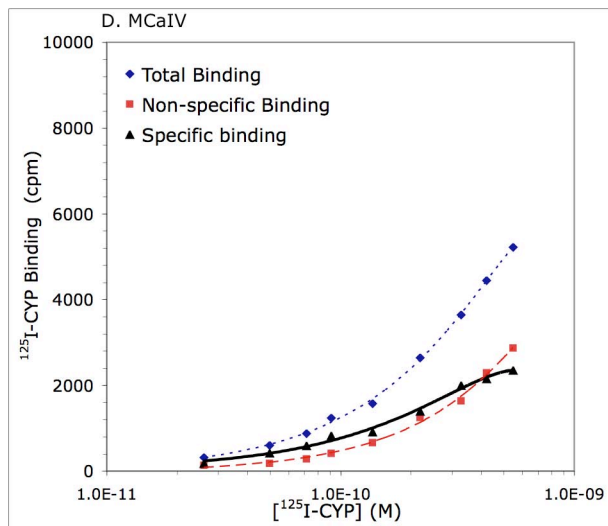
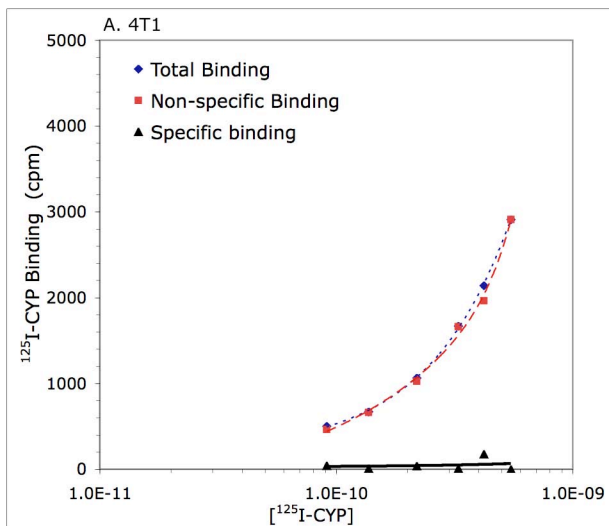
Fig. 5. β -AR agonist-induced VEGF production by MB-231BR is blocked by β -AR antagonists. The response of MB-231BR to varying concentrations of (A) ISO and (B) terbutaline (TERB). (C) The non-selective β -blocker nadolol (NAD) and (D) the β_2 -AR-selective blocker ICI 118,551 (ICI) were added 30 minutes prior to ISO. Cell-free supernatants were harvested after 72 hours in culture and VEGF concentration was determined by ELISA. For all figures, the number of experimental repetitions for each group = 3-6. In (A) and (B), asterisks indicate statistically significant differences versus no β -agonist by Newman-Keuls post-hoc analysis ($p<0.05$). In (C) and (D), asterisks indicate statistically significant differences versus all groups by Newman-Keuls post-hoc analysis ($p<0.05$).

Fig. 6. β -AR activation and cellular proliferation *in vitro*. Proliferation of (A) MB-231BR and (B, C) MB-361 was measured at 72 in culture with and without the non-selective β -AR agonist ISO or the β_2 -AR selective agonist terbutaline (TERB). For β -blockade, MB-361 cells were incubated with the nonselective β -AR antagonist nadolol (NAD) or the β_2 -AR selective antagonist ICI 118,551 (ICI) for 30 minutes prior to addition of the β -agonist. Results from individual experimental repetitions were normalized to percent of 0 ISO/TERB and averaged across 2-5 experimental repetitions. In (B), the asterisk indicates statistical significance relative to all other groups by Bonferroni post-hoc analysis. In (C), the asterisk indicates statistical significance relative to all other groups by Newman-Keuls post-hoc analysis ($p<0.05$).

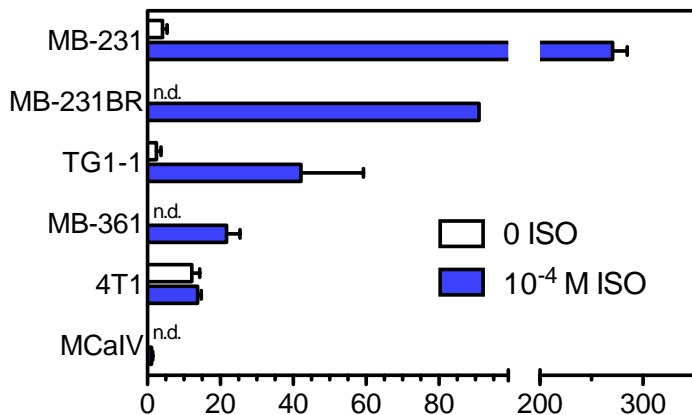
Table 1. Breast Cancer Cell Lines

Cell Line	Species	Cells Isolated from:	Hormone Receptor Expression* (Reference)
MDA-MB-231	Human	Pleural Effusion	ER α ⁻ , EGFR ⁺ , HER2 ^{low} [19, 26]
MDA-MB-231BR	Human	Brain (Nude Mouse)	EGFR ⁺ HER2 ^{lo} [18, 20]
MDA-MB-361	Human	Brain	ER α ⁺ , EGFR ^{low} , HER2 ^{high} [19]
BT474	Human	Breast (Ductal Carcinoma)	ER α ⁺ , EGFR ⁺ , HER2 ^{high} [19]
4T1	Mouse	Spontaneous Mammary Tumor (BALB/c)	[27]
TG1-1	Mouse	Spontaneous Mammary Tumor (FVB/nJ)	HER2 ⁺ [28]
MCAIV	Mouse	Spontaneous Mammary Tumor (C3H)	[29]

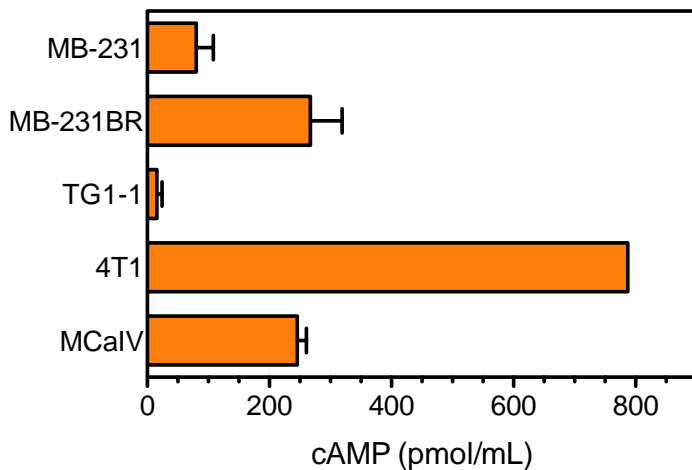
* ER α = Estrogen receptor-alpha; EGFR = Epidermal growth factor receptor

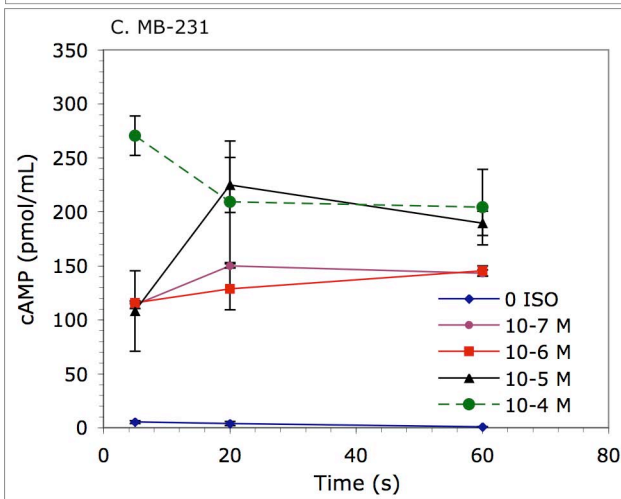
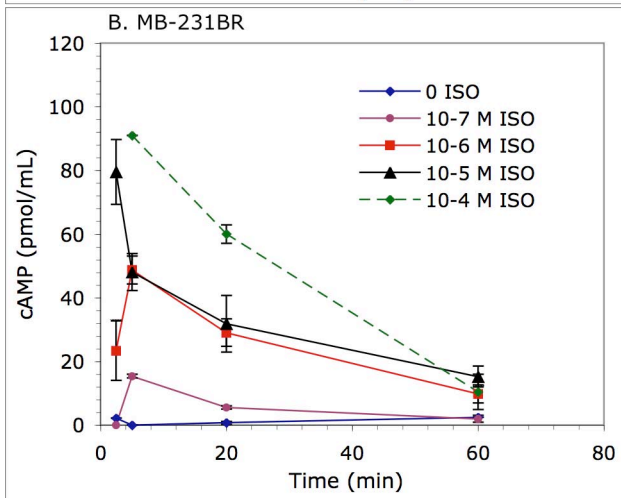
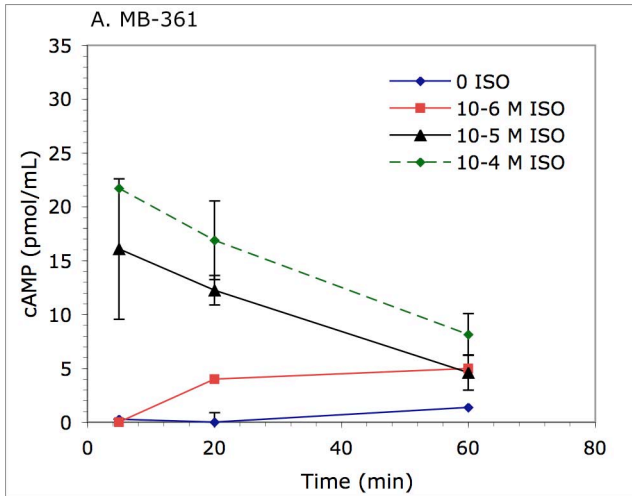


A.

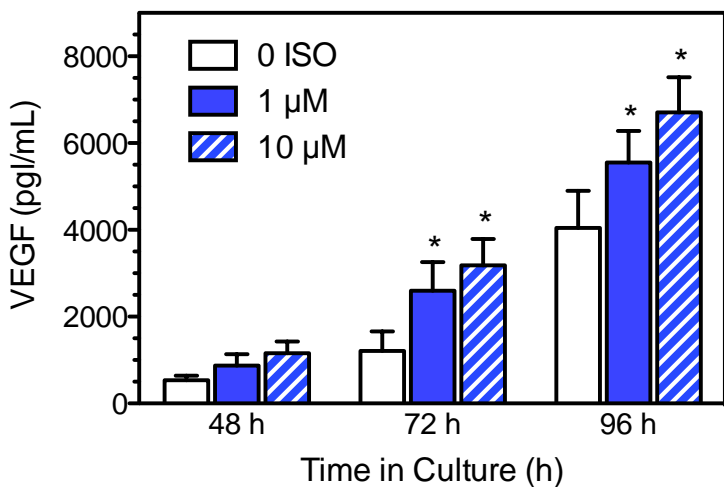


B.

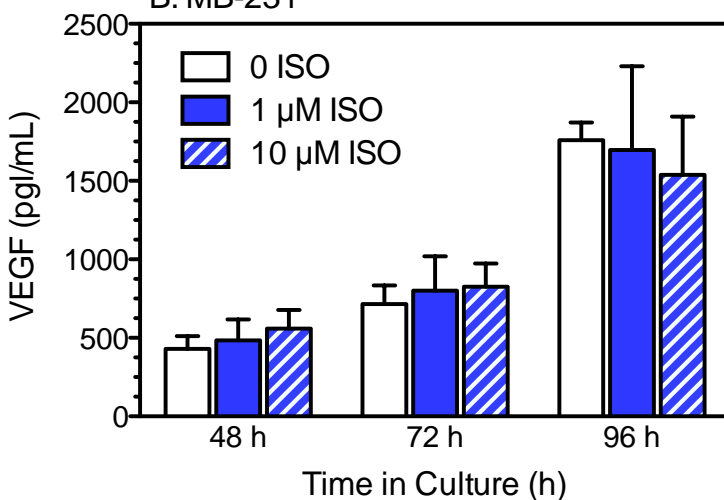




A. MB-231BR



B. MB-231



C. MB-361

